Control Strategies for Machining with Industrial Robots

Sörnmo, Olof

2013

Document Version:
Publisher's PDF, also known as Version of record

Control Strategies for Machining with Industrial Robots

Olof Sörnmo

LUNDS UNIVERSITET

Department of Automatic Control

Department of Automatic Control
Lund University
Box 118
SE-221 00 LUND
Sweden

ISSN 0280–5316
ISRN LUTFD2/TFRT--3261--SE

Printed in Sweden.
Lund 2013

Abstract

This thesis presents methods for improving machining with industrial robots using control, with focus on increasing positioning accuracy and controlling feed rate.

The strong process forces arising during high-speed machining operations, combined with the limited stiffness of industrial robots, have hampered the usage of industrial robots in high-end machining tasks. However, since such manipulators may offer flexible and cost-effective machining solutions compared to conventional machine tools, it is of interest to increase the achievable accuracy using industrial robots. In this thesis, several different methods to increase the machining accuracy are presented. Modeling and control of a piezo-actuated high-dynamic compensation mechanism for usage together with an industrial robot during a machining operation, such as milling in aluminium, is considered. Position control results from experiments are provided, as well as an experimental verification of the benefit of utilizing the online compensation scheme. It is shown that the milling surface accuracy achieved with the proposed compensation mechanism is increased by up to three times compared to the uncompensated case. Because of the limited workspace and the higher bandwidth of the compensator compared to the robot, a mid-ranging approach for control of the relative position between the robot and the compensator is proposed. An adaptive, model-based solution is presented, which is verified through simulations as well as experiments, where a close correspondence with the simulations was achieved. Comparing the IAE from experiments using the proposed controller to previously established methods, a performance increase of up to 56 % is obtained.

Additionally, two different approaches to increasing the accuracy of the machining task are also presented in this thesis. The first method is based on identifying a stiffness model of the robot, and using online force measurements in order to modify the position of the robot to compensate for position deflections. The second approach uses online measurements from an optical tracking system to suppress position deviations. In milling experiments per-

formed in aluminium, the absolute accuracy was increased by up to a factor of approximately 6 and 9, for the two approaches, respectively.

Robotic machining is often performed using position feedback with a conservative feed rate, to avoid excessive process forces. By controlling the applied force, realized by adjusting the feed rate of the workpiece, precise control over the material removal can be exercised. This will in turn lead to maximization of the time-efficiency of the machining task, since the maximum amount of material can be removed per time unit. This thesis presents an adaptive force controller, based on a derived model of the machining process and an identified model of the Cartesian dynamics of the robot. The controller is evaluated in both simulation and an experimental setup.

Acknowledgments

First of all, I would like to thank my supervisors Anders Robertsson and Rolf Johansson, who have been supportive and provided valuable guidance and encouragement. Further thanks go to Klas Nilsson, who has practically been a third supervisor and a great source of ideas. A lot of my research has been performed in close cooperation with Björn Olofsson, and it has been a pleasure both working and traveling with him. Thanks to Karl-Johan Åström for his endless enthusiasm in helping out with everyday control problems.

I would like to thank all my colleagues at the Department of Automatic Control for contributing to a very pleasant environment to work in, especially Anna Lindholm and my office colleagues Andreas Stolt, Josefin Berner, Martin Hast, and Meike Stemmann. Also thanks to Eva Westin, Ingrid Nilsson, Lizette Borgeram, and Monika Rasmusson for help with administrative matters. Leif Andersson, Anders Nilsson, Anders Blomdell, Rolf Braun, and Pontus Andersson have provided valuable assistance with technical issues.

Finally, I would like to thank my fiance Tove and my family for support and guidance.

Financial support is acknowledged from the European Commission's Seventh Framework Programme under grant agreements with the acronyms COMET (Ref. #258769) and SMErobotics (Ref. #287787) as well as the Swedish Foundation for Strategic Research within the program ProViking, under grant ProFlexA PV08–0036. The author is part of the LCCC Linnaeus Center, supported by the Swedish Research Council, and the ELLIIT Excellence Center, supported by the Swedish Government.

Contents

1

Introduction

The topic of this thesis is on how control can improve machining processes performed with industrial robots, with focus on increasing positioning accuracy, and feed rate control.

1.1 Background and Motivation

Industrial robots in the industry of today, *e.g.*, see Figure 1.1, offer cost-efficient and flexible solutions compared to conventional machine tools. The robots are accurately position controlled when moving in free space, suitable for operations such as pick and place, spray-painting, etc. However, when performing tasks that require the robot to come into physical contact with the environment, high accuracy is harder to achieve. The serial structure of the industrial robot and weak gearboxes in the joints, contribute to poor stiffness of the robot end-effector. This limits the achievable positioning accuracy when subject to the strong process forces that occur during machining tasks, such as milling, grinding and deburring. Also, nonlinearities in the joints, such as backlash and friction, further deteriorate the positioning accuracy. Since industrial robots typically only provide measurements of the robot position on the motor side of the joint, any deviations that appear on the arm side cannot be compensated by the robot itself. All of these issues contribute to making machining operations with industrial robots not straightforward to perform [Zhang et al., 2005; Abele et al., 2011]. Therefore, machining has traditionally been performed using dedicated CNC machines, when high accuracy operations are required. This motivates the need for developing new control strategies for improving the accuracy of robotic machining tasks. In this thesis, three approaches to increasing the position accuracy during machining operations are investigated. First, a macro/micro manipulator configuration for compensation of the measured robot deviation is considered. The micro manipulator is modeled and the proposed control architecture is evaluated in a series of milling experiments with the setup. Also, since the

Figure 1.1 A conventional ABB industrial robot.

micro manipulator has a limited workspace, a mid-ranging control scheme is developed for controlling the relative position of the manipulators. Second, a stiffness model of the robot is identified and subsequently used for online deflection compensation using force feedback. Third, an optical tracking system is used to track the robot position and provide feedback to suppress the position deviations.

Another aspect of robotic machining that is considered in this thesis, is how to control the feed rate of the workpiece in order to maximize material removal. If a certain task is to be performed a large amount of times, reductions in cycle-time will generate considerable savings over time. In the case of machining tasks, cycle-time reduction can be achieved by removing as much material per time unit as possible. The limiting factor to the material removal rate is the resulting reaction force that occurs when the machining tool is moved into the workpiece, since a too strong force will break the tool or scorch the workpiece. Thus, it is desirable to strive to always apply the maximum allowed force during machining, which can be achieved by adjusting the feed rate of the workpiece. The reaction force does, however, nonlinearly depend on several time-varying parameters, motivating the need for an adaptive control structure that exercises precise material removal control. In this thesis, modeling of the robot and machining process dynamics, and a subsequent model-based adaptive control structure for feed rate control is presented and verified in both simulations and milling experiments.

1.2 Contributions

The main contributions of this thesis are:

- Modeling and control of an external position compensating micro manipulator, experimentally verified in robotic milling scenarios;
- An adaptive mid-ranging approach to position control of the relative position between the macro and micro manipulator;
- An evaluation of two different deflection compensation schemes for industrial robots;
- An adaptive force control approach to continuously control the feed rate in robotic milling processes.

1.3 Publications

This thesis is based on the following publications:

Olofsson, B., O. Sörnmo, U. Schneider, A. Robertsson, A. Puzik, and R. Johansson (2011). "Modeling and control of a piezo-actuated high-dynamic compensation mechanism for industrial robots". In: *IEEE/RSJ Int. Conf. on Intelligent Robots and Systems*. San Francisco, CA, pp. 4704–4709.

Sörnmo, O., B. Olofsson, U. Schneider, A. Robertsson, and R. Johansson (2012a). "Increasing the milling accuracy for industrial robots using a piezo-actuated high-dynamic micro manipulator". In: *2012 IEEE/ASME Int. Conf. on Advanced Intelligent Mechatronics*. Kaohsiung, Taiwan, pp. 104–110.

Sörnmo, O., B. Olofsson, A. Robertsson, and R. Johansson (2012b). "Increasing time-efficiency and accuracy of robotic machining processes using model-based adaptive force control". In: *10th Int. IFAC Symposium on Robot Control*. Dubrovnik, Croatia, pp. 543–548.

Sörnmo, O., B. Olofsson, A. Robertsson, and R. Johansson (2013). "Adaptive internal model control for mid-ranging of closed-loop systems with internal saturation". In: *IEEE/RSJ Int. Conf. on Intelligent Robots and Systems*. Tokyo, Japan. Submitted.

The first two publications were developed as a cooperation between the author and B. Olofsson, and equal contribution is asserted. This material can also be found in [Olofsson, 2013]. The author was main responsible for the experimental verification and B. Olofsson was main responsible for the modeling and control development. A. Puzik developed the considered compensation mechanism and U. Schneider took part in the implementation and

the experiments. A. Robertsson and R. Johansson provided comments on the manuscripts. The third and fourth publications have the author as main contributor. B. Olofsson assisted with theoretical and technical discussions and together with A. Robertsson and R. Johansson provided feedback on the manuscripts.

1.4 Other Publications

The following publications, in which the author has contributed in related areas, are not part of the thesis:

Lehmann, C., B. Olofsson, K. Nilsson, M. Halbauer, M. Haage, A. Robertsson, O. Sörnmo, and U. Berger (2013). "Robot joint modeling and parameter identification using the clamping method". In: *IFAC Conf. on Manufacturing Modelling, Management, and Control (MIM)*. St. Petersburg, Russia. Accepted for publication.

Olofsson, B., O. Sörnmo, U. Schneider, M. Barho, A. Robertsson, and R. Johansson (2012). "Increasing the accuracy for a piezo-actuated micro manipulator for industrial robots using model-based nonlinear control". In: *10th Int. IFAC Symposium on Robot Control*. Dubrovnik, Croatia, pp. 277–282.

Sörnmo, O., A. Robertsson, and A. Wanner (2012). "Force controlled knife-grinding with industrial robot". In: *2012 IEEE Multi-Conference on Systems and Control*. Dubrovnik, Croatia, pp. 1356–1361.

1.5 Thesis Outline

Chapter 2 introduces an external compensation mechanism for increasing milling accuracy. Modeling and control of the mechanism, as well as an experimental verification in a milling scenario, is also presented in Chapter 2. Chapter 3 presents an adaptive method for performing mid-ranging control of a setup as described in Chapter 2, and the method is evaluated using a smaller scale setup. Deflection compensation using both force and position feedback is presented and evaluated in experiments in Chapter 4. Feed rate control in robotic machining processes is considered in Chapter 5, where an adaptive force control strategy is presented and assessed in milling experiments. Finally, conclusions are drawn in Chapter 6.

2

External Compensation Mechanism

2.1 Introduction

This chapter is based on the publications [Olofsson et al., 2011] and [Sörnmo et al., 2012a].

Within the EU/FP7 project COMET [COMET, 2013], the aim is to increase the accuracy of machining tasks for industrial robots. In particular, milling solutions with an accuracy of less than 50 μm are developed. In order to achieve this, the proposed method is divided into four parts, as displayed in Figure 2.1. This chapter considers the method represented by the green jigsaw-piece in Figure 2.1; "High Dynamics Compensation Mechanism".

For high-precision milling, a three-dimensional piezo-actuated compensation mechanism has been developed [Puzik et al., 2009; Puzik et al., 2010; Puzik, 2011]. The mechanism is to compensate in real-time for the remaining position errors of the robot, which the robot *per se* is unable to compensate for because of its limited structural bandwidth compared to its controlled bandwidth.

The advantages of utilizing an additional manipulator together with a robot in a closed kinematic chain, has been investigated in, *e.g.*, [Sharon et al., 1993], [Sharon and Hardt, 1984]. It was shown that the bandwidth of the endpoint position control loop was increased. The concepts of macro and micro manipulator were introduced to describe the robot and the additional compensation mechanism, respectively. These terms will be adopted in this thesis. Note, however, that the micro manipulator in the proposed experimental setup is not attached to the robot.

Piezo-actuated mechanisms based on flexure-elements have been proposed for micro and nano manipulation, see, *e.g.*, [Li and Xu, 2011; Liaw and Shirinzadeh, 2010]. Although the compensation mechanism considered in this thesis has a similar mechanical design, there are significant differences. Pre-

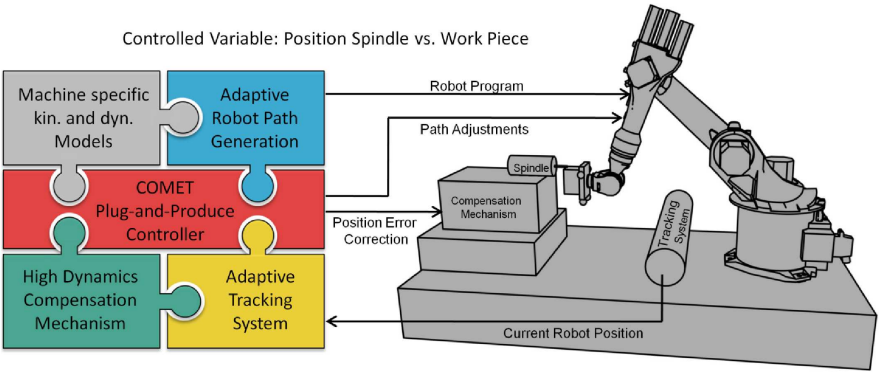

Figure 2.1 The four-part approach to machining of the EU/FP7 COMET-project.

vious designs were designed for compensation in micro and nano manipulation, whereas the micro manipulator discussed in this chapter is designed for machining processes with industrial robots, where strong process forces are required.

In [Vuong et al., 2009], a control scheme for task space control of industrial manipulators, with a hierarchical structure similar to the one utilized for control of the micro manipulator discussed in this thesis, is presented. However, the control of the micro manipulator in this thesis is performed directly in task space, due to the decoupled nature of the actuation mechanism.

This chapter presents a brief overview of the mechanical design of a prototype of the micro manipulator, as well as the experimental setup for performing compensated and uncompensated milling. Further, modeling of the dynamic properties of the micro manipulator and how the subsequent control design should be tuned for satisfactory milling results, is presented. It is shown how nonlinear effects in the mechanism can be handled, and how oscillations that occur due to the resonant mechanical construction can be reduced by using appropriate control design methods. An experimental verification of the proposed control scheme for machining with industrial robots is performed, presenting results from milling tasks in aluminium. The experimental verification contrasts the milling accuracy using the compensation mechanism to the standard uncompensated case.

2.2 Micro Manipulator

Mechanical design

The micro manipulator design has been discussed in several earlier publications, *e.g.*, [Puzik et al., 2009; Puzik et al., 2010; Puzik, 2011], and therefore,

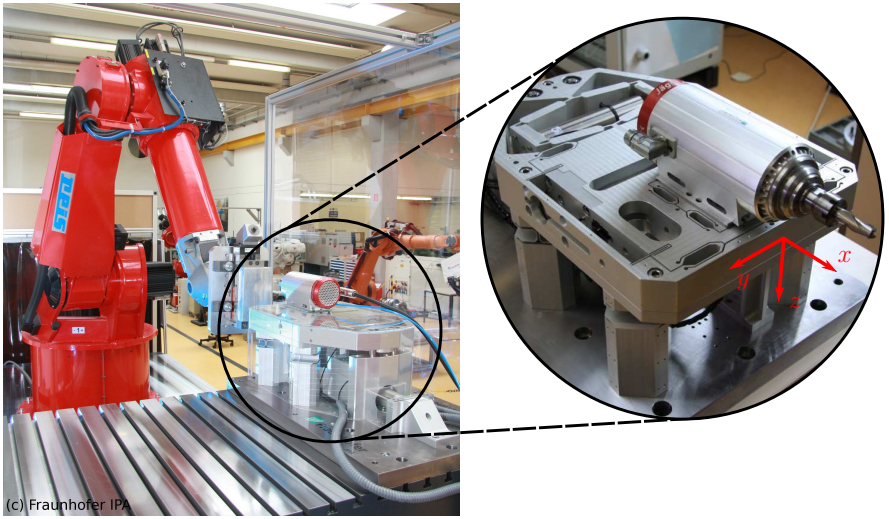

Figure 2.2 The experimental setup for real-time compensation of positioning errors during machining operations, where the robot holds the workpiece and the milling spindle is attached to the micro manipulator. A close-up of the micro manipulator, as seen from the opposite side, is displayed to the right in the figure.

the mechanical design is only briefly described below.

In the proposed setup, the spindle with the milling tool is attached to the micro manipulator and the robot is holding the workpiece, see Figure 2.2. The design of the micro manipulator is such that motion of the machining spindle is possible in all three Cartesian directions. Referring to Figure 2.2, the axes are hereafter called x, y, and z, respectively. The mechanism is actuated by piezo-actuators, whose movements are transferred to a corresponding translational movement of the spindle *via* a flexure mechanism (Figure 2.3).

The flexure mechanism is designed such that the gear ratio of the displacement of the spindle and the extension of the piezo-actuator is approximately five in each direction. This realizes a compensation range for the machining spindle of approximately 0.5 mm in each Cartesian direction.

Actuation and sensors

The extensions of the piezo-actuators are changed by applying voltages, and the extensions are measured using strain gauges, attached to the actuators. The Cartesian displacement of the end-effector plate of the micro manipulator is measured using capacitive sensors, one in each direction.

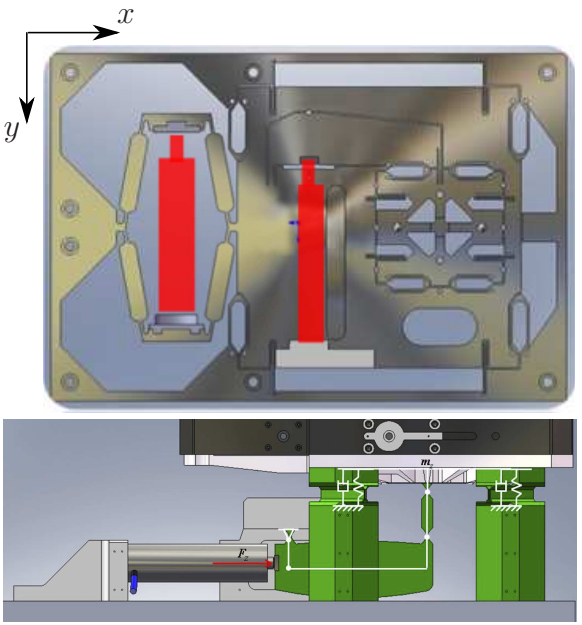

Figure 2.3 Actuation principle for the x-, y-, and z-axes of the micro manipulator. The piezo-actuators are marked by red color in the top drawing [Puzik et al., 2009].

Interface

In order to develop the control structure for the micro manipulator-unit, all sensors and actuators are integrated using a dSPACE system of model DS1103 [dSPACE GmbH, 2007]. Using the software ControlDesk, the user can implement control strategies in a simple manner as well as develop graphical user interfaces. The proposed control design has been implemented in MATLAB Simulink, then generated to C–code using the *Real-Time Workshop* toolbox [MathWorks Inc. 2010]. The compiled C–code is installed in the dSPACE system and executed at a sampling frequency of 10 kHz.

2.3 Identification and Modeling

Due to the inherent resonant character of mechanical systems and the nonlinear effects that appear in piezo-actuators, accurate position control of the micro manipulator without oscillations is a challenging control problem. A model-based solution is here pursued in order to control the tool position.

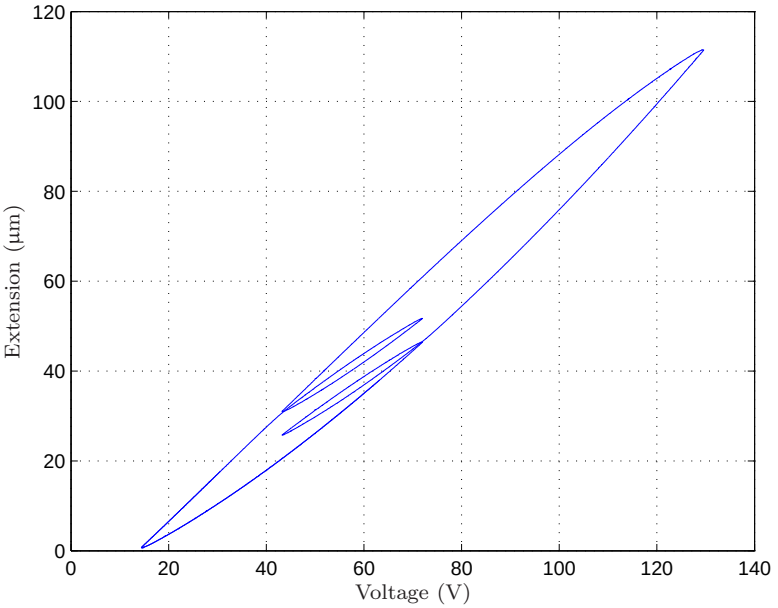

Figure 2.4 Extension of the piezo-actuator as function of the input for a triangular wave with varying amplitude as input.

Nonlinear phenomena in the piezo-actuators

Experiments have been performed on the micro manipulator in order to determine the effect of the nonlinear phenomena in the piezo-actuators. The experiments indicated that the main nonlinearities that need to be handled are hysteresis and the creep phenomenon. Results from experiments where the voltage to the piezo-actuators are alternatingly increasing and decreasing are shown in Figure 2.4. It is obvious that the hysteresis needs to be handled actively for accurate positioning. It is also noted that the hysteresis is both rate and amplitude dependent. Further, experiments showed that the nonlinear creep phenomenon in the actuator is a much slower process than the hysteresis, and thus easier to handle.

Although different in nature, both of these nonlinear effects can be handled using high-gain feedback. The control design will be described in Section 2.4.

Frequency characterization of the mechanical design

In order to characterize the frequency properties of the mechanical design, several frequency response experiments have been performed. The frequency

spectra in the different directions, displayed in Figure 2.5, were estimated using the periodogram method. An important property of the system is the location of the first natural eigenfrequency. It is noted that the characteristics are quite different in the three Cartesian directions. In particular, two natural eigenfrequencies are visible in the x- and z-axes, whereas only one is visible in the y-direction. The first eigenfrequency appears in the frequency range 33–47 Hz in all of the three axes.

The locations of the eigenfrequencies are important since they limit the achievable bandwidth, *i.e.*, how fast the position control loop can be made, in the final closed-loop control system. Increasing the bandwidth beyond the resonance frequency requires a large amount of control actuation and the sensitivity to model errors is increased.

Modeling of the mechanical construction

In order to design control algorithms, it is advantageous to perform modeling of the micro manipulator prior to the design. Two different methods for modeling can be chosen. Firstly, modeling based on mechanical relations can be established, where the design specific parameters are either analytically calculated or experimentally determined.

The other approach is to consider black-box input-output models without investigating the internal mechanical design. This is a common approach in model-based control, which results in satisfactory control performance given that the model captures the essential dynamics of the system. The black-box approach is used in this thesis for modeling of the micro manipulator.

Identification based on black-box models

Using system identification methods [Johansson, 1993], mathematical models describing the micro manipulator can be determined. The axes are assumed to be decoupled, since individual movement of the axes was shown to result in negligible displacement in the other axes. Consequently, each axis is considered as a system with one input and one output. Identification of the models was done in the System Identification Toolbox [Ljung, 2010] in MATLAB, and the State space Model Identification (SMI) toolbox [Haverkamp and Verhaegen, 1997] for identification of state-space models.

Accordingly, consider discrete-time state-space models of the innovations form

$$x_{k+1} = \Phi x_k + \Gamma u_k + K e_k \tag{2.1}$$

$$y_k = C x_k + D u_k + e_k \tag{2.2}$$

where $u_k \in \mathbb{R}^m$ is the input, $x_k \in \mathbb{R}^n$ is the state vector, $y_k \in \mathbb{R}^p$ is the output, e_k is a noise sequence and K is the Kalman gain. The matrices $\{\Phi, \Gamma, C, D\}$ in the state-space representation are identified using one of the

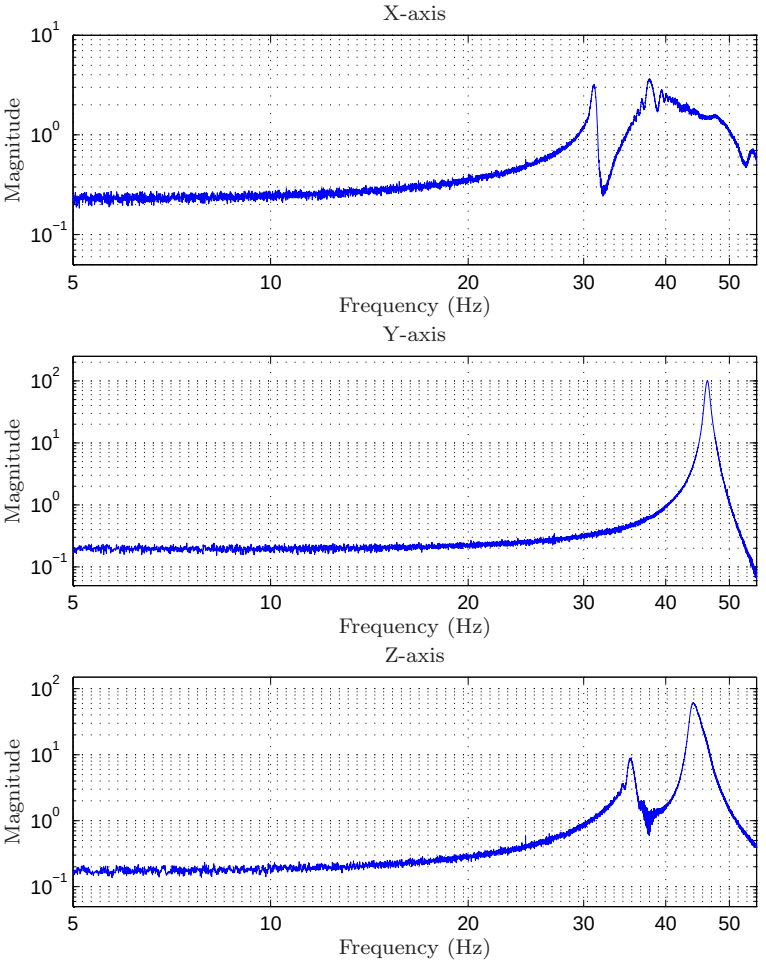

Figure 2.5 Estimated power spectral densities in the Cartesian directions of the micro manipulator.

available implementations of subspace-based identification methods, such as the N4SID-method [Overschee and De Moor, 1994] and the MOESP algorithm [Verhaegen and Dewilde, 1992]. During the identification of the models, a Kalman gain vector for a minimum variance estimate of the states in the model is also determined, based on the noise properties.

Collection of input-output data

The collection of experimental input-output data was performed such that the input u_k is considered to be a scaled version of the input voltage to the actuator, whereas the output y_k is defined to be the position of the spindle as measured by the capacitive sensor.

When performing system identification, an appropriate input signal has to be chosen for experiment design, such that the system is excited properly. A chirp-signal was chosen—*i.e.*, a sinusoid with constant amplitude and linearly increasing frequency—as input, since this signal gives excitation in a well-defined frequency range. Consequently, the start and end frequencies in the chirp-signal have to be chosen based on the frequency range of interest. Given the frequency spectra displayed in Figure 2.5, a suitable range of excitation is 10–60 Hz, see Chap. 8 in [Johansson, 1993].

Model-order selection and preprocessing of the data

When performing identification of the state-space models, a model order has to be chosen. To this purpose, the singular values calculated during the identification procedure using the N4SID or MOESP algorithms are utilized. By plotting these singular values, the gap between the model and the noise level is identified. Based on this information, a sufficient model order can be chosen.

Prior to the identification, the input-output data is processed, such that the mean and the linear trend are removed. Also, the data, which is acquired at 1 kHz, is decimated six times to a sample rate of approximately 167 Hz, which is suitable given the location of the eigenfrequencies in the different axes.

Identified models

Experimentally identified discrete-time state-space models of the form (2.1)–(2.2) in the x, y, and z-directions of the open-loop system were estimated. All models are of the same format. However, the model orders vary in different directions, reflecting the number of natural eigenfrequencies, *cf.* the frequency spectra in Figure 2.5. The model orders are 4, 2 and 5 in the x-, y- and z-directions, respectively. The model order selection was based on the singular values analysis during the identification procedure. The frequency spectra of the identified models are shown in Figure 2.6, and the pole-zero maps of the

models in the x- and y-directions are displayed in Figures 2.7 and 2.8. It is noted in the Bode diagrams that there is good correspondence with the estimated periodograms in Figure 2.5. A measure of the fit of the models to the data, are the *variance accounted for* (VAF) values [Johansson, 1993]. These numbers are 92.5, 99.5 and 97.1 for the identified models in the x-, y- and z-directions, respectively. This indicates that the models capture the essential dynamics of the system.

2.4 Control Architecture

The proposed control architecture for the macro manipulator and the micro manipulator is displayed in Figure 2.9. It consists of three main components; the macro manipulator controller, a tracking system and the micro manipulator controller.

Macro manipulator controller

The macro manipulator, *i.e.*, the industrial robot, is controlled by a conventional robot controller. The path to be tracked is planned offline and any deviation from this path during the milling process is detected by an online tracking system and subsequently compensated by the micro manipulator.

Tracking system and path deviation detection

An optical system is utilized for tracking of the workpiece, which is, in the proposed setup, held by the macro manipulator. As a prototype tracking system, a laser-based sensor is utilized for tracking of the position of the workpiece. However, any optical tracking system with sufficient resolution and sample rate can be utilized. Sufficient resolution in this context is determined by the desired milling accuracy.

The position of the workpiece, as measured by the tracking system, is compared to the nominal position calculated in the macro manipulator controller. Deviations from the nominal path are fed to the micro manipulator controller.

Micro manipulator controller

The position control of the compensation mechanism is handled by the micro manipulator controller. Based on the reference value calculated by the tracking system, the controller positions the micro manipulator, and consequently the attached machining tool. The control problem of the micro manipulator can be divided into two parts. First, the nonlinear effects of the piezo-actuators need to be reduced. Second, the oscillatory mechanical structure needs to be accurately position controlled. The proposed control design is described below.

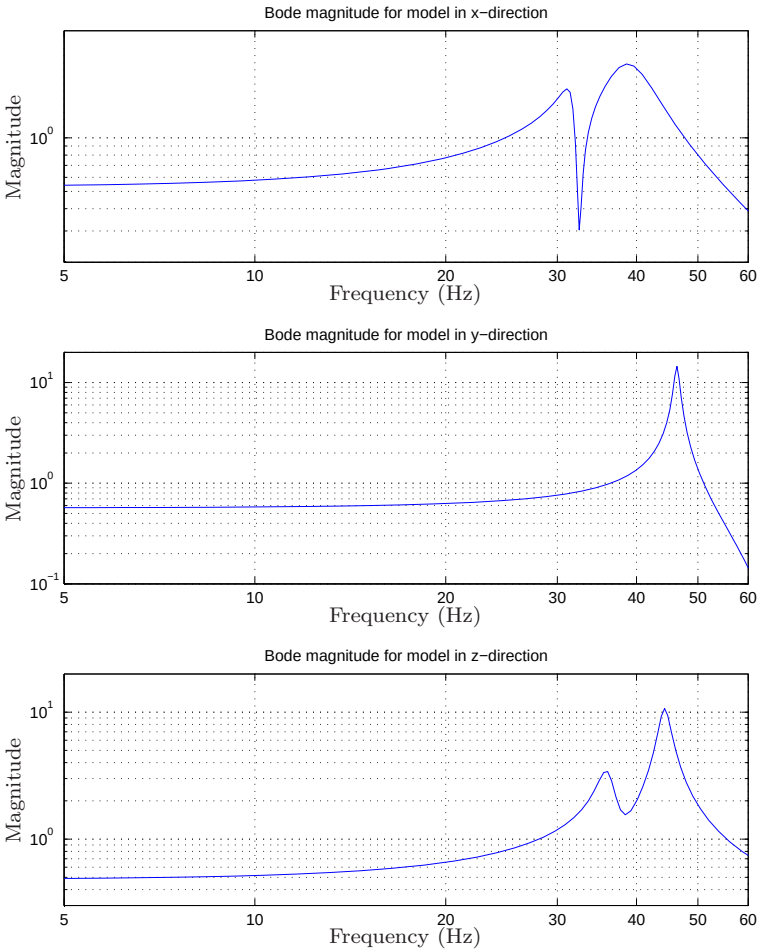

Figure 2.6 Bode magnitude of the discrete-time state-space models identified using subspace identification, in the x-, y- and z-directions, respectively.

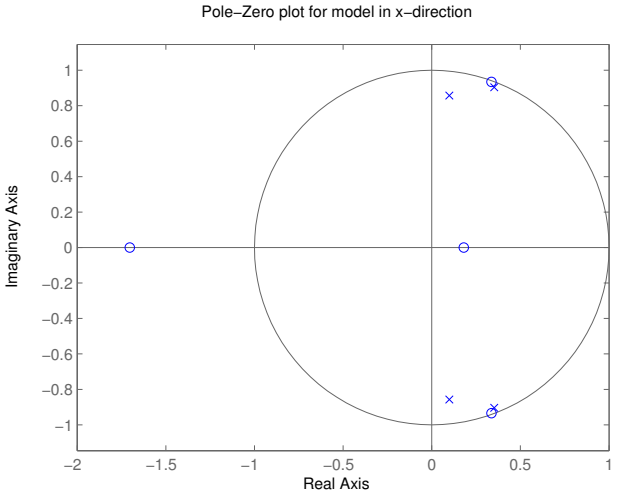

Figure 2.7 Pole-zero map of the model in the x-direction of the micro manipulator.

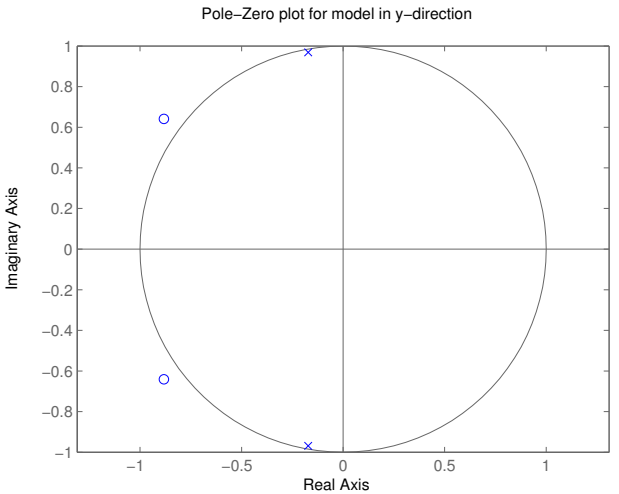

Figure 2.8 Pole-zero map of the model in the y-direction of the micro manipulator.

Inner piezo-actuator control loop

Nonlinear systems can be controlled by both model-based feedforward control and with feedback control. Several approaches to modeling the hysteresis and subsequent model-based control design have been presented in literature, such as the Prandtl-Ishlinskii model and the Preisach model, *e.g.*, [Al Janaideh et al., 2009; Ge and Jouaneh, 1996; Krejci and Kuhnen, 2001]. However, as the extensions of the piezo-actuators in the micro manipulator are available for measurement with the strain gauges, a more straightforward solution is chosen, where an inner feedback loop is closed around the nonlinear actuator. The prototype controller is a PID controller, with continuous-time transfer function

$$G_C(s) = K_p + \frac{K_i}{s} + \frac{sK_d}{1 + sK_d/N} \tag{2.3}$$

where K_p, K_i and K_d are controller parameters. The derivative part in the controller is lowpass filtered, in order to reduce the amplification of high-frequency noise contaminating the measured signal from the strain gauge. The cutoff frequency in the lowpass filter is determined by the parameter N. The PID controller also has to be accompanied by an anti-windup scheme, to handle the case when the controller saturates the actuators. Discretization of this continuous time controller for implementation in the dSPACE system is straightforward [Åström and Wittenmark, 1997].

The purpose of the inner PID controller is to linearize the nonlinear effects in the piezo-actuators, as well as minimize the influence of load disturbances. This can be achieved by increasing the proportional gain K_p and the integral gain K_i as much as possible, while still maintaining desired stability and sensitivity properties. It will be shown by experimental results in Section 2.6, that this approach—*i.e.*, using a linear controller for reducing the nonlinear effects in the piezo-actuator—results in satisfactory performance of the control of the piezo-actuators.

Model-based feedback control of the micro manipulator

By utilizing the identified state-space models, a state feedback control loop can be designed for each of the three Cartesian directions of the micro manipulator. However, new models need to be identified after closing the inner feedback loop around the piezo-actuators, where the reference signal to the inner PID control loop is considered as the input instead. This is necessary in order to reduce modeling errors that were caused by the nonlinear dynamics in the initial dynamic characterization. However, since the difference compared to the open loop models presented in the previous section is negligible, the models with the closed inner loop are not presented here.

Since the micro manipulator is a highly oscillative system with large resonance peaks, state feedback is an appropriate control structure, as damping

can be introduced in the construction by suitable control design. The control law for state feedback control of the system (2.1)–(2.2) can be stated as follows

$$u_k = -Lx_k + u_{ff} \tag{2.4}$$

where the parameter vector L is to be chosen and u_{ff} is the feedforward control signal. The design procedure is to determine the L-vector by linear-quadratic (LQ) optimal control [Åström and Wittenmark, 1997], *i.e.*, such that the cost function

$$J(x,u) = \sum_{k=1}^{\infty} x_k^T Q x_k + u_k^T R u_k \tag{2.5}$$

where the matrices Q and R are user defined weights in the optimization, is minimized.

Since all states in the state-space model of the micro manipulator are not available for measurement, a Kalman filter is introduced for estimation of the states [Kalman, 1960], based on the measured position signal and the identified model. The Kalman filter is organized as [Åström and Wittenmark, 1997]

$$\hat{x}_{k+1} = \Phi\hat{x}_k + \Gamma u_k + K(y_k - C\hat{x}_k - Du_k) \tag{2.6}$$

$$\hat{y}_k = C\hat{x}_k + Du_k \tag{2.7}$$

where the estimated states $\hat{x}_k$ and the estimated output $\hat{y}_k$ have been introduced. Since the identified model is based on experimental data, where the mean is subtracted from the real data, a *disturbance state* is added to the observer, *i.e.*, a new, constant state

$$\hat{x}_{k+1}^e = \hat{x}_k^e \tag{2.8}$$

is introduced. By adding this state, the correct static gain for the estimation is achieved [Åström and Wittenmark, 1997]. The model identification procedure provides the Kalman gain vector K for estimation of the states in the model. The corresponding pole placement is also used in the Kalman filter with the disturbance state, but with an additional pole corresponding to the introduced disturbance state.

The control law for the state feedback control is then based on the estimated states, *i.e.*, $u_k = -L\hat{x}_k + u_{ff}$. In order to remove possible stationary errors in the position control loop, integral action is introduced in the state feedback. This is done by extending the state vector with the integral state

$$x_i(t) = \int_0^t (r(\tau) - y(\tau))\ \mathrm{d}\tau \tag{2.9}$$

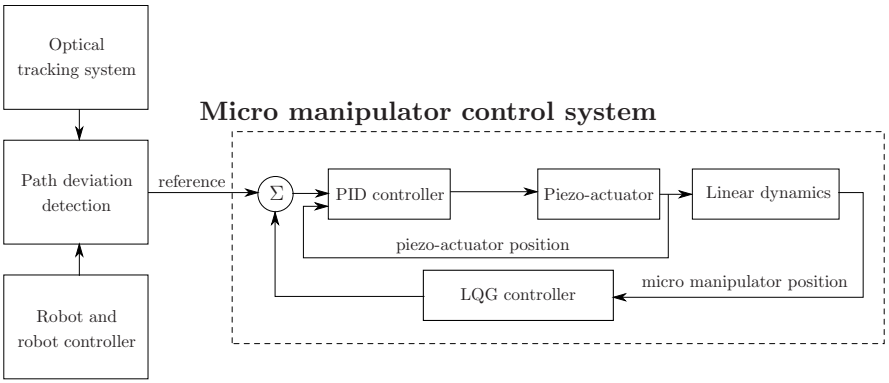

Figure 2.9 Control architecture for online compensation of position errors during milling operations with industrial robots. The micro manipulator control scheme positions the machining tool based on the reference value calculated as the deviation of the robot from the nominal path.

where the reference signal $r(t)$ has been introduced. With this extra state, it is also required that the state feedback vector L is augmented with one element, *i.e.*, $L_e = \begin{bmatrix} L & l_i \end{bmatrix}$, where l_i is the integral gain. Also, note that the integral state needs to be discretized prior to design and implementation in the dSPACE system.

Different approaches can be chosen to handle the feedforward control signal. In the scheme presented in this thesis, the feedforward control u_{ff} is chosen as a direct term from the reference signal, $u_{ff} = l_r r_k$. The parameter l_r determines the static gain of the closed-loop system and is tuned such that the gain is 1. The final control structure is summarized in the block diagram in Figure 2.9.

Tuning of controller parameters

In order to determine the state feedback vector L, the weight matrices Q and R in the LQ design need to be determined. Based on the identified model for the micro manipulator in the y-direction, the characteristics of the closed-loop system were investigated for different weight matrices. Especially, the choice of the weight R in relation to the matrix Q, determines the "aggressiveness" of the controller. Bode diagrams of the closed-loop system for different choices of R, where the Q matrix has been chosen as the identity matrix, can be seen in Figure 2.10. The direct term l_r in the control law has been chosen such that the static gain for the closed-loop control system is equal to one in all cases. It is noted that a lower weight results in a more aggressive controller, where the resonance in the system is well damped, at the cost of reduced bandwidth. Hence, the controller needs to be tuned as a trade-off

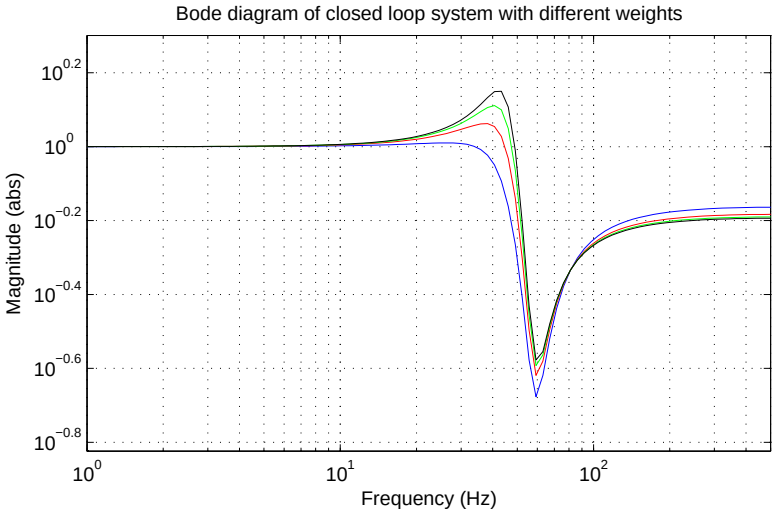

Figure 2.10 Bode diagram for the closed-loop system for $Q = I$ and different choices of the R-matrix in the LQ-design. The choices of R are 1.0, 2.0, 3.0 and 4.0 for the blue, red, green and black line, respectively.

between the attenuation of the poorly damped resonance in the system and the "aggressiveness" of the controller. A too aggressive controller may result in unsatisfactory control performance, due to *e.g.*, high noise sensitivity or poor accuracy of the identified process model.

Outlier detection

In order to make the measurements from the laser-based tracking system more robust, an outlier detection scheme is utilized in the micro manipulator controller. Outliers appear in the measurements in the current setup because of aluminium chips that are emitted from the milling process, obscuring the laser beam and resulting in a temporary deviation from the correct measurement. Even though the outliers are infrequent, they have to be handled actively. Therefore, an online outlier detection scheme with prediction of measurements [Menold et al., 1999], was implemented in the controller.

2.5 Experimental Setup

The experimental evaluation was performed using a REIS industrial robot of model RV40 [Reis GmbH, 2011] with a maximum payload of 40 kg, as the macro manipulator. The spindle was attached to the micro manipulator and the macro manipulator held the workpiece, which in this case was a

block of aluminium (AlMg3,5). The setup is such that both face milling and peripheral milling, also referred to as radial milling, can be performed, see Figure 2.2.

Sensors

To the purpose of measuring the deflections of the robot perpendicular to the milling direction, *i.e.*, the deflections which were to be compensated by the micro manipulator, a Keyence laser sensor of model LK-G87 [Keyence Corp. 2006], with a resolution of 0.2 μm was used as tracking system.

Compensated and uncompensated milling

In order to illustrate the benefit of the micro manipulator, the milling experiments were performed both in a setting where compensation with the micro manipulator was utilized and in a setting with the spindle rigidly attached to a fixed base. In the latter setup, no compensation is performed. The two experimental settings are displayed in Figure 2.11.

In the experiments without compensation, the robot configuration was mirrored, with respect to the center plane of the robot, compared to the configuration chosen in the experiments with compensation. Consequently, the compliance properties of the macro manipulator in the two configurations are equivalent, which is important in order to make the compensated and uncompensated milling results comparable.

2.6 Position Control Experiments

Several experiments were performed in order to evaluate the performance of the control design. Firstly, the PID controllers for the nonlinear piezo-actuators were tuned, in order to achieve as high performance as possible. An important aspect to consider in the control scheme is if the nonlinear effects in the piezo-actuators influence the frequency characteristics of the micro manipulator. To this purpose, the quadratic coherence spectrum $\gamma_{uy}(\omega)$ [Johansson, 1993], given by

$$\gamma_{uy}(\omega) = \frac{|S_{uy}(i\omega)|^2}{S_{uu}(i\omega)S_{yy}(i\omega)}, \tag{2.10}$$

where $S_{uy}(i\omega)$ is the power cross-spectrum between input u and output y, $S_{uu}(i\omega)$ and $S_{yy}(i\omega)$ are the autospectra for u and y, respectively, is investigated. The coherence spectra for the x-, y-, and z-directions of the micro manipulator are displayed in Figure 2.12.

It is observed that the relation between input and output in the x-, y- and z-directions appears to be linear within the frequency range of interest, *i.e.*,

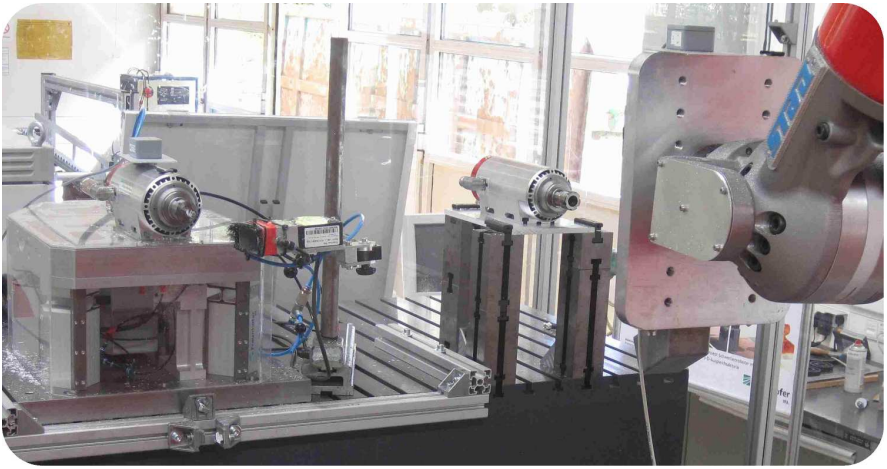

Figure 2.11 Experimental setup for evaluation of the effectiveness of the proposed micro manipulator, which is seen to the left. The machining spindle to the right is rigidly attached to the base. This setup is utilized for milling experiments without compensation.

below the resonance frequencies visible in Figure 2.5. Only around the resonance frequencies can the coherence be observed to be below one, and thus linear modeling will be a less accurate description of the dynamics at these frequencies. However, since the major part of the frequency range exhibit a linear relation, the proposed approach is considered feasible.

In order to experimentally evaluate the control design on the experimental setup, a reference signal was recorded as the position deflection of the robot during a milling operation in one dimension, measured with the laser sensor. The recorded signal corresponds to the deflection of the robot in the milling direction, which in this case equals the y-direction of the micro manipulator.

Experiments were performed on the real setup with varying weight matrices Q and R. Also, the integral state was added to the state feedback, whose influence is determined by the parameter l_i. The weights $Q = I$ and $R = 2.5$, where I is the identity matrix, was found to result in satisfactory control performance.

The reference signal is filtered using a notch filter, where the notch is located at the eigenfrequency of the micro manipulator in the y-direction, as observed in the frequency spectrum in Figure 2.5. This is done in order not to excite the mechanical resonance in the construction. Another option is to low-pass filter the reference signal. However, since the construction itself is of low-pass character, frequencies above the natural eigenfrequency in the reference signal will be attenuated.

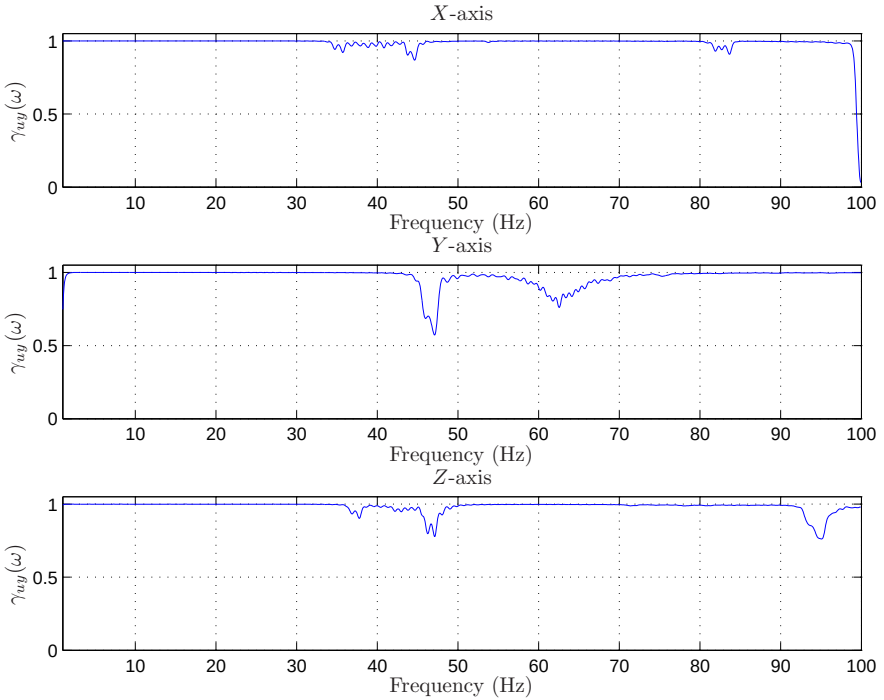

Figure 2.12 Estimated coherence spectra with the inner PID control loop active, in the x-, y-, and z-directions of the micro manipulator.

The recorded signal was applied as reference signal in the y-direction of the micro manipulator. Figure 2.13 shows the control performance of the inner PID controller loop. It is noted that the control error with this reference signal, which contains high frequencies, is within approximately ± 3 µm. Figure 2.14 shows the spindle position, as measured by the capacitive sensor. The figure indicates satisfactory control performance, with a control error of within approximately ± 15 µm.

It is observed in Figure 2.14 that the control error signal exhibits periodic behavior of different frequencies. The frequency spectrum of this signal is displayed in Figure 2.15. Three peaks at 9, 140, and 250 Hz are clearly visible. The first peak corresponds to the eigenfrequency of the robot and the higher frequencies are related to eigenfrequencies of the piezo-actuator, the rotation of the spindle and the impact of the milling tool on the workpiece. Further, it is noted that the first significant eigenfrequency of the micro manipulator in the y-direction at 47 Hz is well damped as a result of the control design.

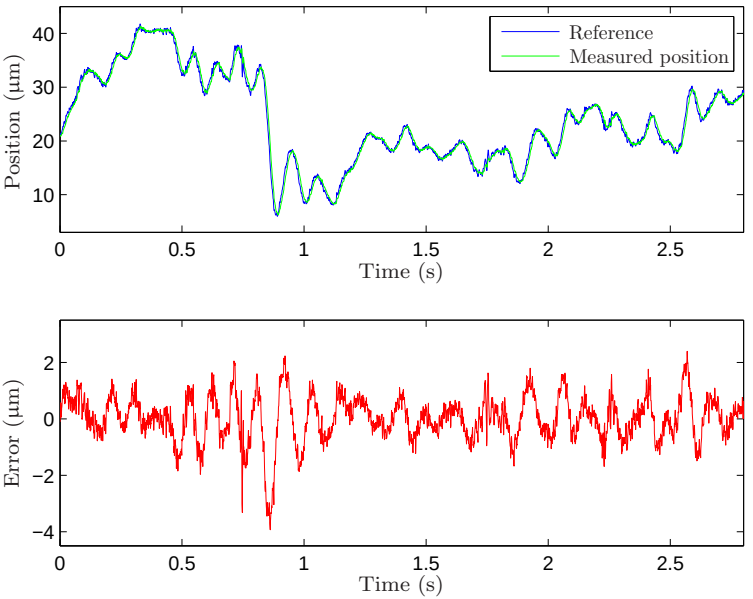

Figure 2.13 Control performance in the inner PID control loop in the y-direction.

2.7 Milling Experiments

With the experimental setup described in Section 2.5, milling in aluminium was performed. The macro manipulator can be reconfigured such that milling can be executed in all three directions of the micro manipulator. Results obtained during face milling in the x-direction and peripheral milling in the y- and z-directions of the micro manipulator are presented. The experiments were performed with a feed rate of 7.5 mm/s, a spindle speed of 28 000 rpm and a depth-of-cut of 1 mm in the face millings and 1×10 mm^2 in the peripheral millings.

Milling experiments with compensation

***X*-direction** In the first setting, face milling is performed, where the surface orthogonal to the x-axis of the micro manipulator is to be machined. Consequently, the micro manipulator is controlled in this direction. The result of the milling experiment is displayed in Figure 2.16. The control error is defined as the difference between the reference value to the micro manipulator control system and the measurement from the capacitive sensor in the

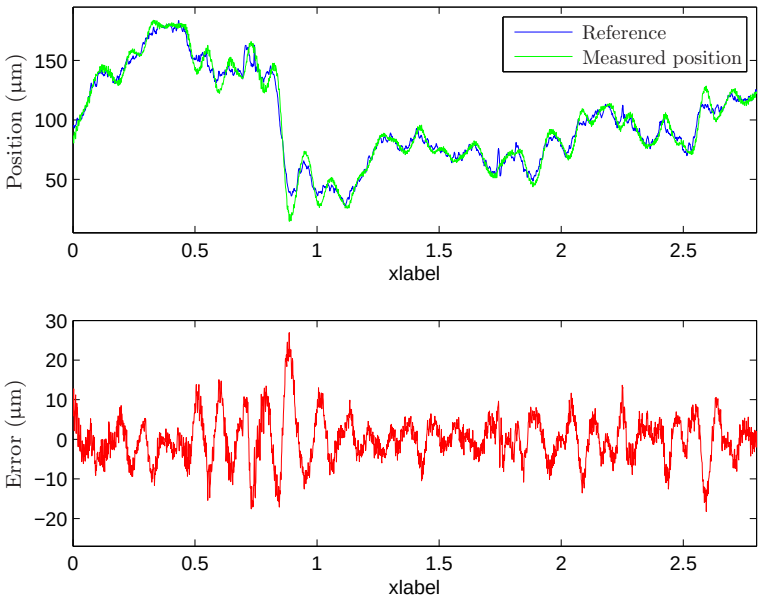

Figure 2.14 Performance of the model-based spindle positioning control in the y-direction.

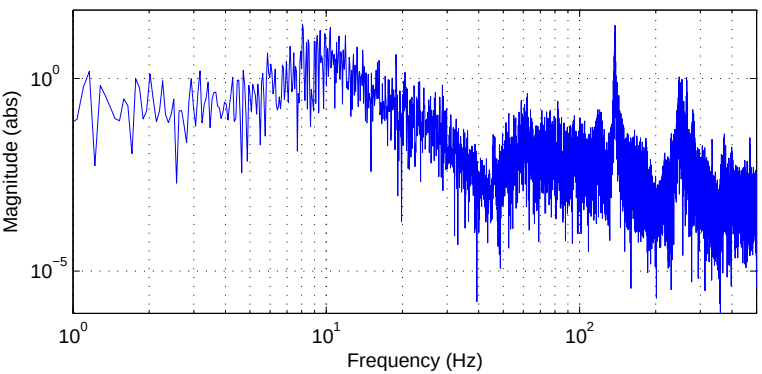

Figure 2.15 Spectrum of the control error signal from Figure 2.14.

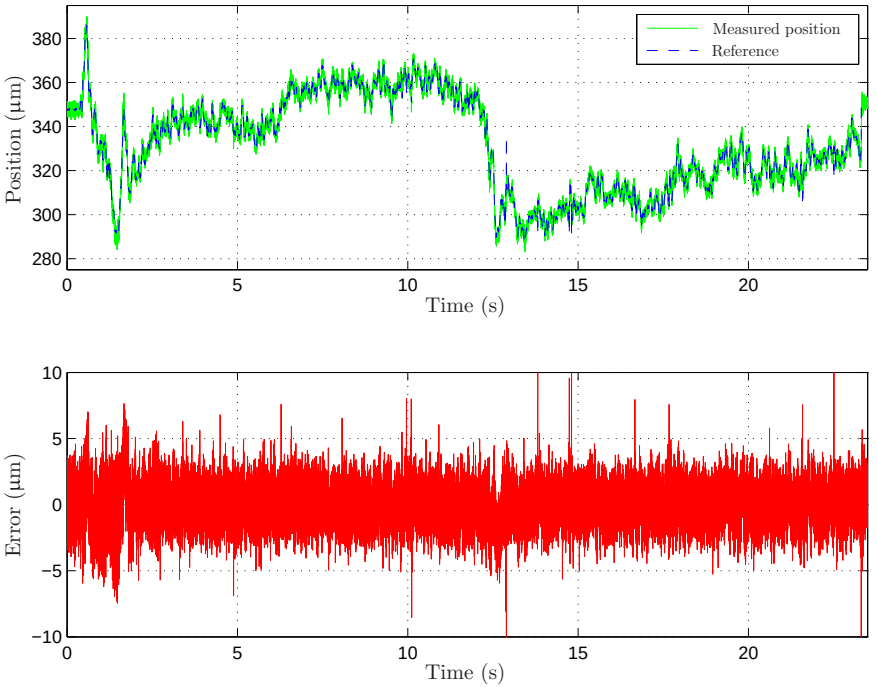

Figure 2.16 Reference and position of the micro manipulator during milling experiment in the x-direction (upper panel) and corresponding control error (lower panel).

x-direction of the micro manipulator.

***Y*-direction** The milling accuracy has further been tested in a peripheral milling, where the compensation was performed in the y-axis of the micro manipulator. It should be noted that this milling task is different from the face milling presented in the previous paragraph, in the sense that the process forces affect the macro manipulator differently.

Furthermore, the experiment is designed such that the macro manipulator, on purpose, is not moving perpendicularly to the compensation direction. This situation can be considered as a result of a poorly calibrated workpiece or industrial robot. By utilizing the micro manipulator, this effect can be compensated since the movement of the macro manipulator is tracked in real-time. The result of the milling experiment is displayed in Figure 2.17. The control error displayed is defined analogously to the case with face milling in the x-direction of the micro manipulator.

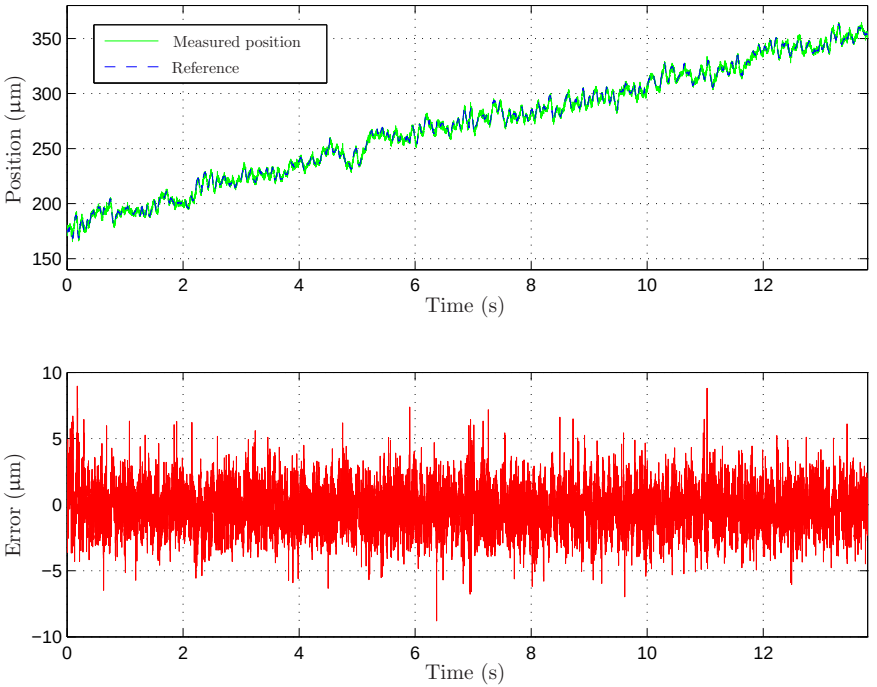

Figure 2.17 Reference and position of the micro manipulator during milling experiment in the y-direction (upper panel) and corresponding control error (lower panel).

***Z*-direction** The third experiment was a peripheral milling along the z-axis of the micro manipulator. The control performance of the micro manipulator in the milling experiment is displayed in Figure 2.18.

Milling experiments without compensation

The same milling experiments described and presented in the previous subsection were repeated, but with the machining spindle rigidly attached—*i.e.*, no online compensation was active. The results of the experiments will be evaluated in the subsequent section.

Experimental evaluation

Frequency analysis of control error From a control theory point of view, the results obtained from the milling experiments should be evaluated by examining if there is more information available in the control error—

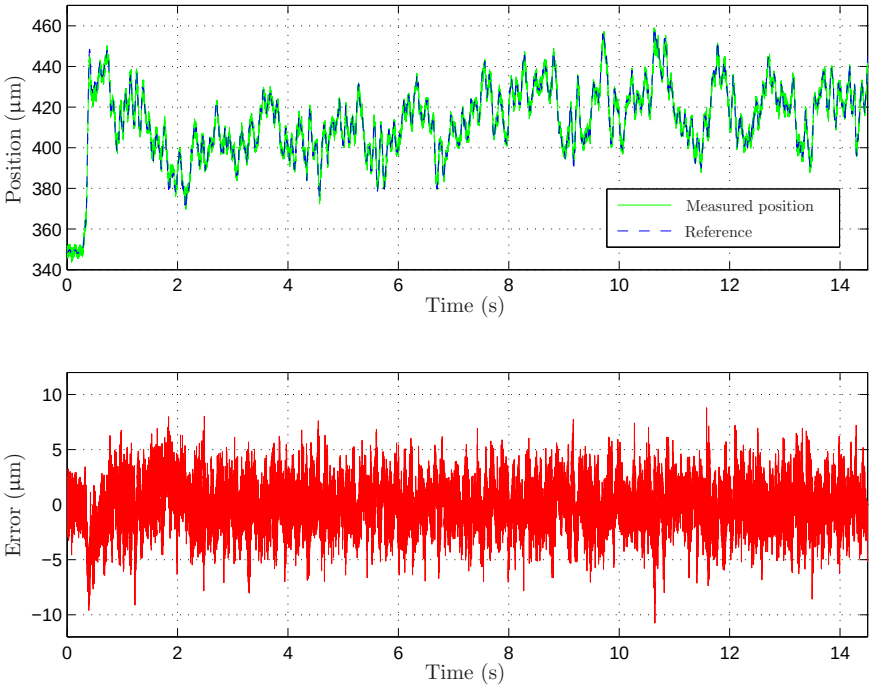

Figure 2.18 Reference and position of the micro manipulator during milling experiment in the z-direction (upper panel) and corresponding control error (lower panel).

i.e., separating the noise in the measurements from the possibly available information, which should be acted upon.

To this purpose, frequency spectra of the control errors are estimated using Welch's method [Johansson, 1993]. The estimated power spectral densities (PSD) for the control error in the performed milling experiments are displayed in Figure 2.19. The spectra are further discussed in Section 2.8.

Measurement of milling profiles

Since the main objective of the milling experiments is to achieve a high accuracy of the machined surface on the workpiece, a Mahr measurement device of model M400 SD26 [Mahr GmbH, 2011] was utilized to measure the surface roughness of the obtained profiles. The measurement device is calibrated such that it has a measurement accuracy below 1 µm.

Milling with compensation The results of the surface roughness measurements, for the three milling experiments with online compensation, are

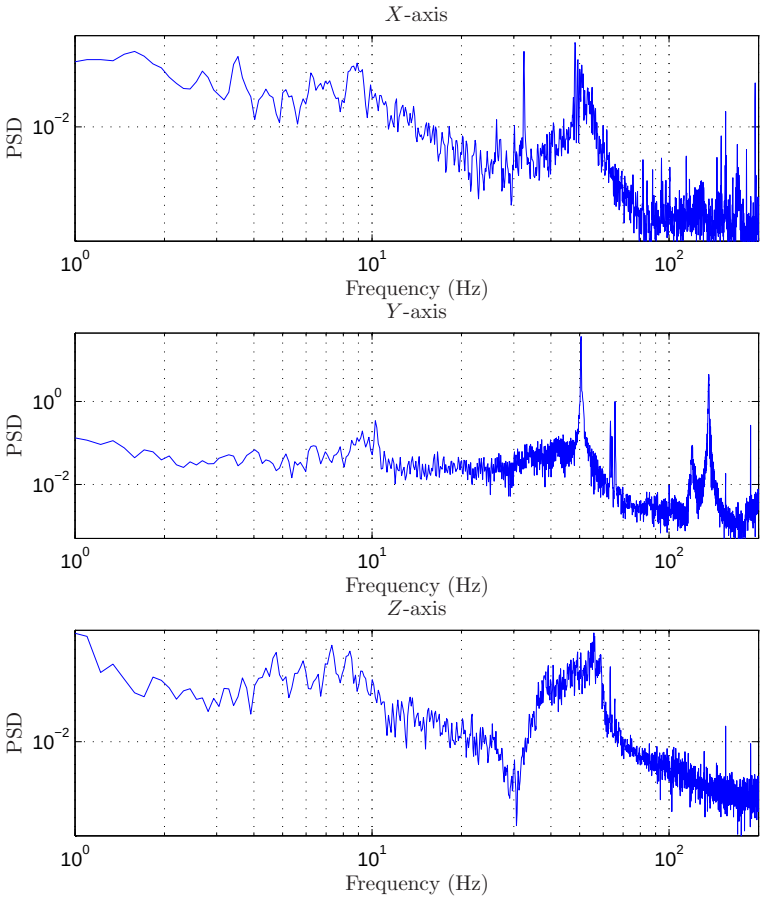

Figure 2.19 Estimated power spectral densities for the control error in all directions of the micro manipulator.

Table 2.1 Maximum error e_m of milling profiles.

Axis	e_m compensated (µm)	e_m uncompensated (µm)	Ratio
x	14.0	18.3	1.3
y	12.8	29.3	2.3
z	24.5	67.0	2.7

Table 2.2 Standard deviation σ_e of milling profiles.

Axis	σ_e compensated (µm)	σ_e uncompensated (µm)	Ratio
x	2.8	7.6	2.7
y	2.5	5.6	2.2
z	4.7	14.9	3.2

displayed in Figure 2.20. The measured profiles indicate that the milling accuracy in the x- and y-directions are within ± 7 µm and that the error of the measured milling profile is within approximately ± 12 µm in the z-direction of the micro manipulator. Furthermore, it is noted that the measured profiles correspond well to the measurements from the capacitive sensors attached to the micro manipulator, which are used for feedback. This correspondence indicates that the measured position of the compensation mechanism agrees with the actual position of the milling tool. Photos of the milled surfaces for the experiments in the x-, y-, and z-directions are provided in Figures 2.22–2.24.

Milling without compensation The resulting surface roughness of the profiles from the uncompensated milling experiments, as measured by the Mahr device, is displayed in Figure 2.21. To evaluate the quality of the measured profiles from the experiments with online compensation compared to the profiles obtained in milling without compensation, both the maximum error e_m and the standard deviation σ_e of the profiles are calculated. Table 2.1 shows the maximum errors of the profiles, calculated as the minimum value subtracted from the maximum value, and Table 2.2 shows the standard deviations from the nominal profiles.

2.8 Discussion

This chapter has investigated modeling and control of a piezo-actuated compensation mechanism. The developed control structure was realized in a discrete-time implementation and experimentally verified by performing posi-

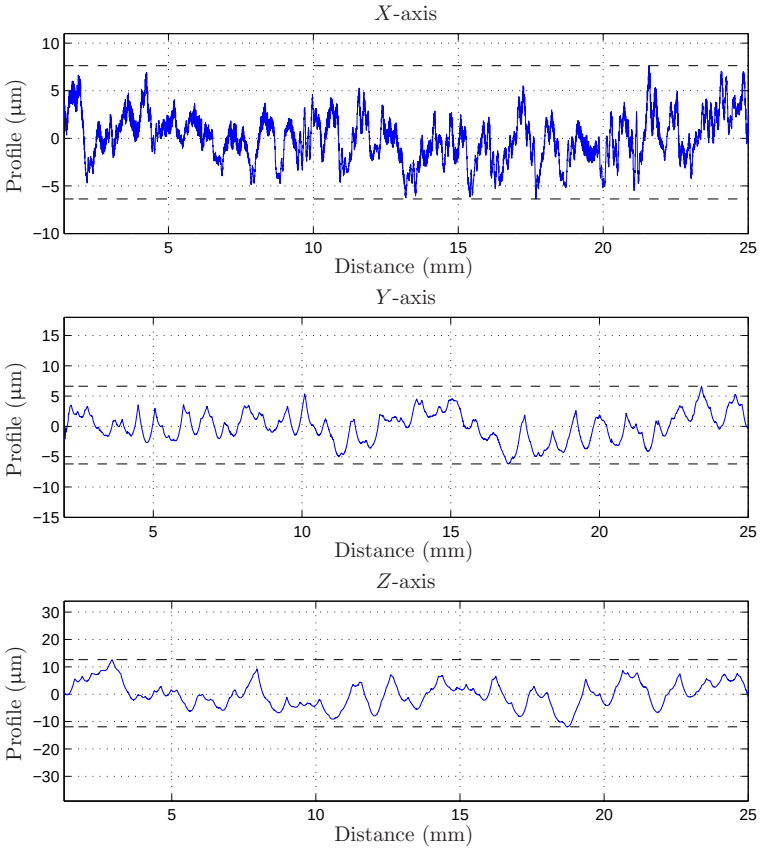

Figure 2.20 Workpiece profiles after face milling in x-direction and peripheral milling in y- and z-directions of the micro manipulator. In all experiments online compensation with the micro manipulator was utilized.

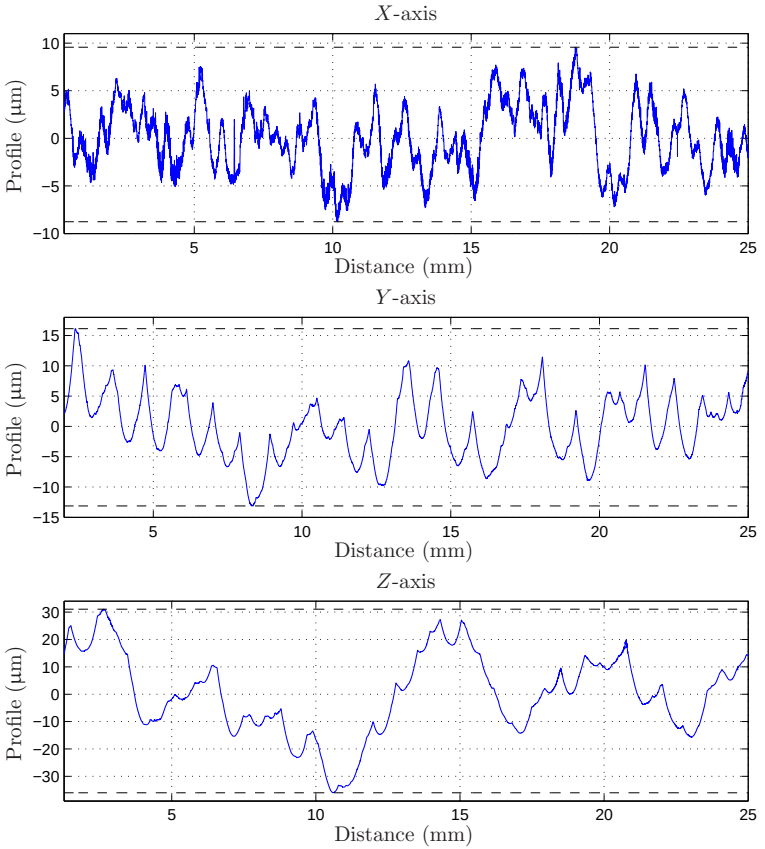

Figure 2.21 Workpiece profiles after uncompensated milling in the x-, y-, and z-directions of the micro manipulator, respectively.

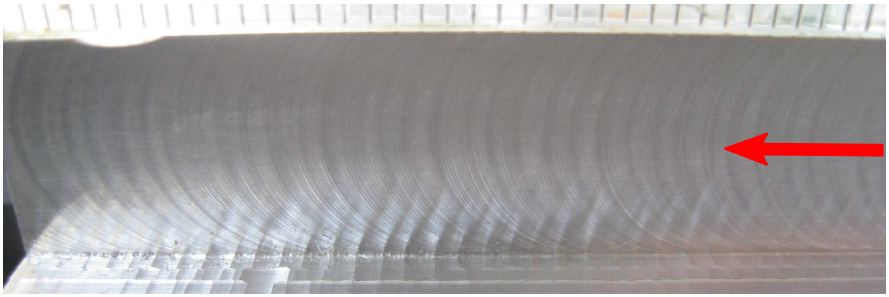

Figure 2.22 Workpiece after face milling on the surface indicated by the red arrow, with compensation in the x-direction of the micro manipulator.

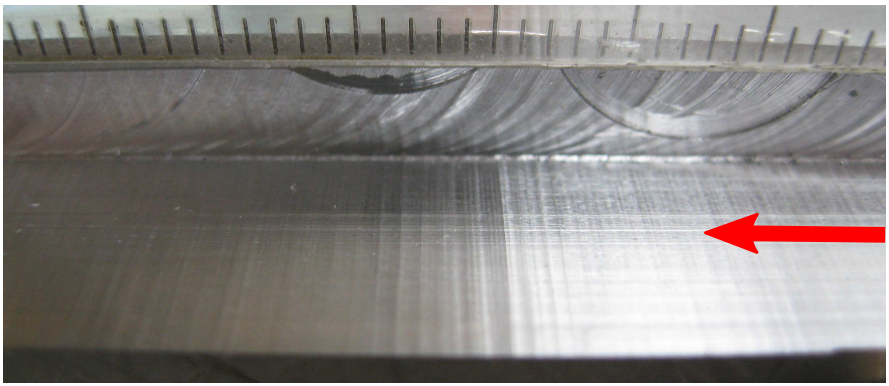

Figure 2.23 Workpiece after peripheral milling on the surface indicated by the red arrow, with compensation in the y-direction of the micro manipulator.

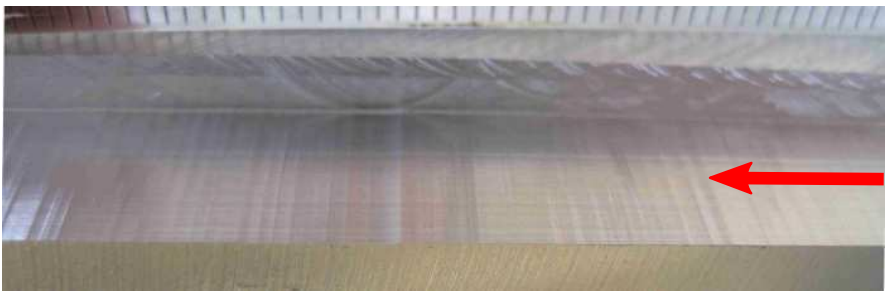

Figure 2.24 Workpiece after peripheral milling on the surface indicated by the red arrow, with compensation along the z-direction of the micro manipulator.

tion control and milling experiments using the micro manipulator. By tuning the state feedback controller appropriately, damping was introduced in the mechanical construction by control design. The resulting control error for the reference signal recorded during a milling operation was within approximately ± 15 µm, which by far achieves the desired accuracy of 50 µm for the complete milling task. Further, from the results presented in Tables 2.1 and 2.2, it is evident that online compensation with the micro manipulator has improved the milling accuracy significantly compared to the uncompensated case. From the experimental evaluation, it can be concluded that both the maximum error and standard deviation of the measured milled surface profiles has been reduced by up to a factor of 3. It is, however, to be noted that these measurements only describe the surface accuracy of the workpiece, not the absolute accuracy. This means that the displacements in robot position that occur due to process forces are not reflected in this evaluation. Should the absolute accuracy be considered, the increase of accuracy using the proposed method would be significantly greater, since the micro manipulator can compensate for the unwanted position displacements.

It is further noted that the increase in accuracy is greater in the y- and z-directions, than in the x-direction. This can be explained by the fact that face milling was performed in the x-direction, as opposed to peripheral milling in the y- and z-directions, which are different in that how the milling process forces affect the robot. If milling was to be performed in a stiffer material than aluminium, such as steel, the process forces would be considerably higher, and the accuracy increase using the proposed method would most likely be greater.

Several observations are made in the frequency analysis of the control error. All frequency spectra of the control errors in Figure 2.19 exhibit peaks at approximately 10 Hz and at 50 Hz. The latter is a disturbance from the power network system. The former relates to the eigenfrequencies of the industrial robot in the corresponding Cartesian directions. This is experimentally confirmed by modal analysis of the REIS RV40 robot [Schneider, 2010]. However, while the peaks are visible, they are not prominent. This suggests that the micro manipulator controller can attenuate the most important disturbance during the milling—*i.e.*, the natural eigenfrequencies of the robot.

The achievable bandwidth of the position controller for the industrial robot is limited by the natural eigenfrequencies of the mechanical structure and the non-colocated sensing and actuation—*i.e.*, joint-based actuation and task space measurements of the position of the workpiece [Fasse and Hogan, 1995]. The advantage of utilizing the proposed micro manipulator is the significantly increased bandwidth of the end-effector position control, which is the result of the colocation of the actuation—with the micro manipulator—and the task space sensors [Sharon et al., 1993]. In the current experimental setup, the bandwidth of the micro manipulator is 3–4 times higher than that

of the macro manipulator.

Further, the influence of the mechanical design of the micro manipulator on the milling performance is visible in the spectra of Figure 2.19. The zero in the z-direction of the micro manipulator at 30 Hz is clearly visible in the corresponding frequency spectrum. Likewise, one of the natural eigenfrequencies of the micro manipulator in the x-axis at 32 Hz is visible. The bandwidth of the closed-loop position controller for the micro manipulator is consequently limited by the mechanical design.

3

Adaptive Mid-Ranging Control

3.1 Introduction

This chapter is based on the publication [Sörnmo et al., 2013].

In the setup for performing high-precision milling that was presented in the previous chapter, the focus was on control of the micro manipulator. However, since the proposed micro manipulator only has a workspace of approximately 0.5mm in each axis, the manipulator may reach its actuation limits when performing advanced milling tasks. Thus, a mid-ranging control approach is proposed in this chapter, for controlling the relative position between the manipulators in a macro/mini scenario.

Mid-ranging is a control strategy that is useful for the case when two actuator systems control the same variable, such as flow or position, and one of the systems is faster and possibly more accurate, but has a limited working range. The idea is then to utilize both systems to control the desired variable, making use of the higher bandwidth of the fast system, while keeping its position close to the midpoint of its working range, in order not to reach its limits [Allison and Isaksson, 1998].

In order to achieve a system that is robust to process parameter variations, which may occur because of the strong process forces of the milling process and varying cutting conditions, it is desirable to employ an adaptive control structure. However, in the scenario considered in this chapter, the two manipulators are already controlled closed-loop systems which contain internal input saturations, which does not render the design of an adaptive mid-ranging controller straightforward. Motivated by this, an adaptive internal model control scheme for mid-ranging control is presented, with adaptive dynamic reference governors for compensation of internal saturations, making the control approach possible.

A set of different mid-ranging control strategies are evaluated in [Allison and Isaksson, 1998], based on, *e.g.*, Valve Position Control (VPC) and Model Predictive Control (MPC). Design and tuning guidelines of VPC and Modified VPC controllers (MVPC) are presented in [Allison and Ogawa, 2003]. Anti-windup schemes for VPC controllers are introduced in [Haugwitz et al., 2005].

Internal Model Control (IMC) is reviewed and compared with similar control strategies in [Garcia and Morari, 1982], where also several IMC stability theorems are proven and practical tuning guidelines are provided. An extension of IMC to nonlinear systems is presented in [Economou et al., 1986], where it is proven that the properties of linear IMC also applies to the general nonlinear case. The problem of having a control signal saturation for an IMC controller is considered in [Zheng et al., 1994]. Design and stability analysis of Adaptive Internal Model Control (AIMC) is provided in [Datta and Ochoa, 1996], and the discrete-time counterpart is described in ["Adaptive internal model control: the discrete-time case"]. Nonlinear approaches to AIMC are investigated in [Hu and Rangaiah, 1999], as well as in [Hunt and Sbarbaro, 1991], where neural networks are utilized.

The application of mid-ranging control using IMC is investigated in [Gayadeen and Heath, 2009], where design rules are presented and verified through simulation studies.

Discrete-time Dynamic Reference Governors (DRG) for constrained nonlinear systems is considered in [Bemporad, 1998], and reference governors for systems with input and state saturations are presented in [Gilbert et al., 1995].

The method presented in this chapter is based on [Gayadeen and Heath, 2009], which is here extended by introducing adaptivity to the IMC mid-ranging structure, inspired by [Datta and Ochoa, 1996] and ["Adaptive internal model control: the discrete-time case"]. Further, the control scheme is modified to account for internal saturations, by introducing a dynamic reference governor based on the concepts of [Gilbert et al., 1995], but derived using a different approach. Further, in order to maintain performance under parameter variation, the DRG is made adaptive, and compensation for estimation errors is introduced to ensure robustness to process variation.

3.2 Method

Consider two stable, discrete-time closed-loop systems on the standard feedback form, see Figure 3.1, denoted $H_{cl}^{f}(z)$ and $H_{cl}^{s}(z)$, representing the micro and macro manipulator, respectively. Consequently, the bandwidth of $H_{cl}^{f}(z)$ is significantly higher than that of $H_{cl}^{s}(z)$. The controllers in the closed-loop systems are assumed known, and the output signals of the closed-loop

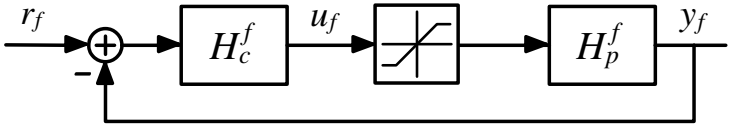

Figure 3.1 Block diagram for the standard feedback form with input saturation to the process. In this figure, $H_{cl}^f(z)$ is displayed.

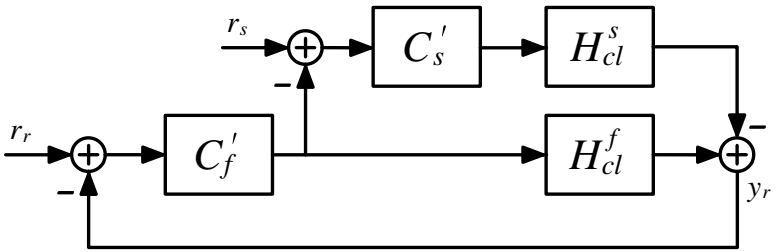

Figure 3.2 Block diagram for the VPC and MVPC mid-ranging control structures.

systems, denoted y_f and y_s, are measured. The midpoint of the micro manipulator workspace is zero.

The objective to perform mid-ranging control of the two closed-loop systems can be met by standard methods such as VPC control, as described in [Allison and Isaksson, 1998] and [Allison and Ogawa, 2003]. The block diagram for the VPC scheme is constructed as displayed in Figure 3.2, where y_r is the relative position of the manipulators, r_r the desired relative position and r_s the desired setpoint of the mid-ranged input. It is to be noted that in this study, since the midpoint of the micro manipulator is zero, the input r_s is also zero and will hence be disregarded.

The structure of the controllers $C_f'(z)$ and $C_s'(z)$ can be chosen arbitrarily, but are commonly selected as PI controllers. Experimental tuning of the controllers is tedious work and even with accurate models of the process, arbitrary pole-placement is not always possible. Internal Model Control is an appealing solution which has been proven to yield satisfactory results in mid-ranging scenarios [Gayadeen and Heath, 2009]. However, as mentioned earlier, the process parameters may change over time and it is therefore desirable to adapt the IMC controller in order to correct for the process changes.

The block diagram for the mid-ranging IMC is displayed in Figure 3.3, where C_f and C_s are the controllers, $\hat{H}_{cl}^f$ and $\hat{H}_{cl}^s$ the internal models of

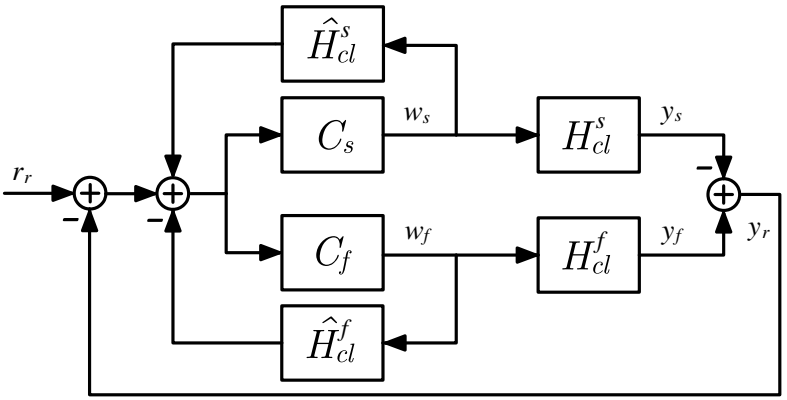

Figure 3.3 Block diagram for the IMC mid-ranging control structure.

H^f_{cl} and H^s_{cl}, respectively. It is to be noted that the notation C_f and C_s represent Q_1 and Q_2 respectively, in the Youla-parametrization of the IMC, according to [Gayadeen and Heath, 2009]. The complementary sensitivity function $T_f(z)$ is introduced as the desired response of the system from r_r to y_r, and $T_s(z)$ is the desired response of the system from r_r to y_r with $w_f = 0$. In order to achieve the desired mid-ranging effect, the following conditions for the controllers must be fulfilled:

$$T_f(z) = C_f(z)H^f_{cl}(z) - C_s(z)H^s_{cl}(z) \tag{3.1}$$

$$T_s(z) = C_s(z)H^s_{cl}(z). \tag{3.2}$$

The controllers are thus calculated as

$$C_f(z) = \frac{T_f(z) + T_s(z)}{H^f_{cl}(z)} \tag{3.3}$$

$$C_s(z) = \frac{T_s(z)}{H^s_{cl}(z)} \tag{3.4}$$

where the parameters of $H^f_{cl}(z)$ and $H^s_{cl}(z)$ should be updated in order to adapt the controllers. For this purpose, a Recursive Least Squares (RLS) algorithm [Johansson, 1993] with forgetting factor $\lambda < 1$ is introduced, because of its fast convergence for input signals of proper excitation, which are assumed to be present. For systems with low excitation, a Kalman filter might exhibit better performance. The proposed method can easily be modified to incorporate a different estimator. The estimator is used to continuously estimate the process parameters of H^f_{cl} and H^s_{cl}, and consequently update the internal models $\hat{H}^f_{cl}$ and $\hat{H}^s_{cl}$, as well as the controllers C_f and C_s. The RLS

algorithm is stated as [Johansson, 1993; Åström and Wittenmark, 1997]:

$$\hat{\theta}_k = \hat{\theta}_{k-1} + K_{k-1}(y_k - \phi_k^T \hat{\theta}_{k-1}) \tag{3.5}$$

$$K_k = P_{k-1}\phi_k(\lambda + \phi_k^T P_{k-1}\phi_k)^{-1} \tag{3.6}$$

$$P_k = \frac{1}{\lambda}(I - K_k\phi_k^T)P_{k-1} \tag{3.7}$$

where P_k is the covariance matrix, K_k a gain matrix, λ the forgetting factor and $\hat{\theta}_k$ is the model parameter estimates from the discrete-time measurement model of the form

$$y_k = \phi_k^T \theta_k + e_k \tag{3.8}$$

where e_k is white noise.

However, as displayed in Figure 3.1, H_{cl}^f contains an internal saturation of the inner control signal u_f (denoted $u_{f,k}$ in this section, where k is current sample), with a given saturation level at $\pm u_{\text{sat}}$. The system H_{cl}^s is assumed not to have an internal saturation. Once the control signal saturates, *i.e.*, when the system leaves its linear region, the linear internal model can no longer accurately describe the process. Further, the estimation of H_{cl}^f will be corrupted as a result of the saturation, since the input/output relation of the plant is no longer linear. This will lead to a false estimate of the system parameters and in turn unexpected behavior, in the worst case instability. This problem may be solved by implementing a nonlinear model and applying nonlinear estimation techniques, which will become intricate, especially if H_{cl}^f is implemented with anti-windup. Instead, an adaptive DRG is introduced to modify the input to the system, so that the system is never allowed to enter saturation. This approach makes linear modeling still feasible. The dynamics of anti-windup schemes possibly implemented in the closed-loop system can be disregarded, since the system is designed to never enter saturation.

Consider the control structure of H_{cl}^f as displayed in Figure 3.1, where the controller and process dynamics are known and given by the rational, discrete-time transfer functions

$$H_c^f(z) = \frac{n_0 + n_1 z^{-1} + ... + n_{a-1} z^{-(a-1)} + n_a z^{-a}}{m_0 + m_1 z^{-1} + ... + m_{b-1} z^{-(b-1)} + m_b z^{-b}} \tag{3.9}$$

$$H_p^f(z) = \frac{q_0 + q_1 z^{-1} + ... + q_{c-1} z^{-(c-1)} + q_c z^{-c}}{p_0 + p_1 z^{-1} + ... + p_{d-1} z^{-(d-1)} + p_d z^{-d}} \tag{3.10}$$

where $[a, b, c, d] \in \mathbb{Z}_0$. The objective is to dynamically modify the reference input $r_{f,k}$ to H_{cl}^f, so that $|u_{f,k}| \leq u_{\text{sat}}, \forall k$. The modified input to the system is denoted $w_{f,k}$, and the dynamic relation between $w_{f,k}$ and $r_{f,k}$ is given by

$$w_{f,k} = w_{f,k-1} + \alpha_k(r_{f,k} - w_{f,k-1}), \tag{3.11}$$

which is a first order low-pass filter with a time-varying parameter α_k. When $\alpha_k = 1$ the filter does not affect the input and $w_{f,k} = r_{f,k}$ holds true, and conversely when $\alpha_k = 0$, $w_{f,k} = w_{f,k-1}$.

When $|u_{f,k}| \leq u_{\text{sat}}, \forall k$, is satisfied, the control signal $u_{f,k}$ is given by

$$u_{f,k} = \frac{H_c^f}{1 + H_c^f H_p^f} w_{f,k} = \frac{\sum_{i=0}^{e} q_i' z^{-i}}{\sum_{i=0}^{f} p_i' z^{-i}} w_{f,k} \tag{3.12}$$

where $e = a + d$ and $f = \max(d + b, a + c)$. In order to determine α_k, the predicted control signal with unaltered reference is denoted by $\hat{u}_{f,k}$ and defined as

$$\hat{u}_{f,k} = u_{f,k}|_{\alpha_k = 1}.$$

If $|\hat{u}_{f,k}| \leq u_{\text{sat}}$, there is no need to alter the input, and thus $\alpha_k = 1$. Otherwise, the desired control signal should be as large as possible, *i.e.*, $\pm u_{\text{sat}}$. The desired control signal in the current time-step k is denoted $u_{f,k}^d$ and defined as

$$u_{f,k}^d = \text{sgn}(\hat{u}_{f,k}) u_{\text{sat}}$$

which together with (3.11) and (3.12) gives the expression for α_k:

$$\alpha_k = \begin{cases} \frac{p_0' u_{f,k}^d + \chi(u_{f,k}, w_{f,k})}{q_0'(r_{f,k} - w_{f,k-1})}, & |\hat{u}_{f,k}| > u_{\text{sat}} \\ 1, & |\hat{u}_{f,k}| \leq u_{\text{sat}} \end{cases} \tag{3.13}$$

where

$$\chi(u_{f,k}, w_{f,k}) = \sum_{i=1}^{f} p_i' z^{-i} u_{f,k} - \sum_{i=1}^{e} q_i' z^{-i} w_{f,k} - q_0' w_{f,k-1}. \tag{3.14}$$

Since the system $H_{cl}^f(z)$ is likely be time-varying, and the inner controller $H_c^f(z)$ is fixed, the inner process $H_p^f(z)$ must be estimated in order to adapt the DRG to the process changes. Since measurements of $u_{f,k}$ are not available, and it is only estimated based on time-invariant models, the process dynamics $H_p^f(z)$ cannot be determined based on the estimations. However, under the assumption that $|u_{f,k}| \leq u_{\text{sat}}, \forall k$, holds true, the inner process of the system can be expressed in terms of $H_{cl}^f(z)$, which is already estimated to adapt the IMC controller, and $H_c^f(z)$;

$$H_p^f(z) = \frac{H_{cl}^f(z)}{H_c^f(z)(1 - H_{cl}^f(z))} \tag{3.15}$$

Using the fact that $y_{f,k}$ is measured and $H_c^f(z)$ is known, real values of past control signals are calculated and used to improve the prediction of $u_{f,k}$, reducing errors that occur because of process variation. In order to further compensate for estimation errors, the difference between the predicted and the real control signal in time-step $k-1$ is used to decrease the saturation limit u_{sat} in the reference governor so that

$$\tilde{u}_{\text{sat}} = u_{\text{sat}} - \max(0, \text{sgn}(\hat{u}_{f,k})(u_{f,k-1} - \hat{u}_{f,k-1})), \tag{3.16}$$

where $\tilde{u}_{sat}$ is the modified saturation limit, and the max-function is added such that $\tilde{u}_{\text{sat}} \leq u_{\text{sat}}$. Since this compensation aims to minimize errors caused by process variation, there is no gain in forming a predictor to compute the control signal in time-step k, because the possibly erroneous model would be used for the prediction.

The scenario of H_{cl}^f and H_{cl}^s being non-minimum phase systems must be considered, since the systems are inverted according to the control design equations (3.3) and (3.4). Inverting non-minimum phase zeros will result in an unstable controller. This can be handled by approximating a stable inverse of the system, by mirroring the non-minimum phase zeros into the unit circle, ensuring stability of the resulting controller. The continuous-time version of the IAE optimal approximation is given in [Wiener, 1949]. The discrete-time counterpart is performed by inverting the magnitude of the zero with unaltered argument, an example of this method is shown in Figure 3.4. The described algorithm is implemented and used in every sample to, if needed, mirror the zeros of the models provided by the estimators.

Before activating the AIMC controller, an initial estimation phase is performed, using a sufficiently exciting signal as input to the systems, until the estimated models have reached the desired accuracy. During this phase, the requirement $|u_{f,k}| \leq u_{\text{sat}}, \forall k$ is unlikely to be fulfilled by the DRG since its prediction model is being estimated. Therefore it is important to choose the excitation signal such that the system does not saturate during this phase.

The final control scheme for the mid-ranging adaptive internal model control with compensation for internal saturation is displayed in Figure 3.5. It is to be noted that the proposed approach can analogously be extended to systems where internal saturations appear in both H_{cl}^f and H_{cl}^s.

In order to evaluate the proposed control scheme, a comparison to existing methods, such as the MVPC structure, is performed. Following the tuning rules given in [Allison and Ogawa, 2003], the controllers C_f and C_s in Figure 3.2, are chosen as PI controllers, and designed using the same desired closed-loop system as for the proposed controller. Since H_{cl}^f contains an internal saturation, and the control signal is not available, the PI controllers will undoubtedly suffer from integrator windup problems. Assuming that the difference between the unsaturated and saturated control signal is available to the controller, a tracking anti-windup algorithm [Haugwitz et al., 2005]

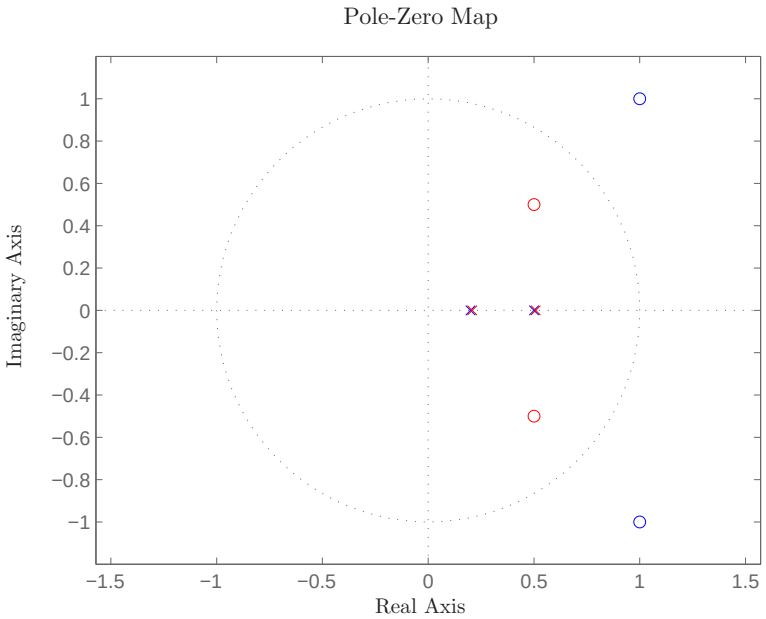

Figure 3.4 Example of mirroring non-minimum phase zeros. The original system is shown in blue, and the mirrored system in red.

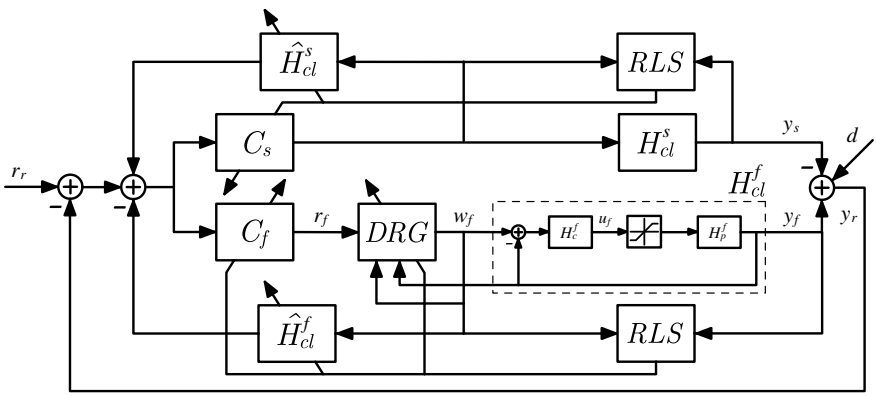

Figure 3.5 Block-scheme for the mid-ranging adaptive internal model control, with internal saturation compensation.

is implemented. Both controllers, with and without anti-windup, denoted MVPC and MVPC+AW, are evaluated in simulation and experiments.

3.3 Simulation Results

The proposed control scheme in Figure 3.5 was implemented and tested in MATLAB Simulink, using $u_{\text{sat}} = 10$ and the following systems:

$$H_c^f(z) = 5, \quad H_p^f(z) = \frac{2hz^{-1}}{1 - z^{-1}}, \quad H_{cl}^s(z) = \frac{1 - e^{-h}}{1 - e^{-h}z^{-1}} \tag{3.17}$$

where h is the sample time of the simulation, in this case $h = 0.004$ s. The desired complementary sensitivity functions are set to

$$T_f(z) = H_{cl}^f(z), \quad T_s(z) = H_{cl}^s(z) \tag{3.18}$$

which corresponds to preserving the bandwidths of the closed-loop systems. This choice is motivated by the assumption that the systems are well-controlled closed-loop systems, ideally having as high bandwidth as possible. An initial guess is provided to the estimators, and the systems are excited using a low amplitude square-wave. In the first simulation, a ramped square-wave with a superimposed low-frequency sine wave is sent as relative position reference r_r and the relative position y_r is subject to a step position disturbance d. The result of the simulation is displayed in Figure 3.6. The ramped input is used to demonstrate the mid-ranging effect of the micro manipulator system position y_f, which is clearly visible from the bottom panel in Figure 3.6, where the green curve is kept close to its midpoint. Further, it can be concluded that H_{cl}^f never enters saturation, since the control signal u_f, which is the unsaturated control signal, is kept within the saturation bounds. It is also noted that the position disturbance at 18 s is attenuated rapidly, similar to the response of the closed-loop system. This is expected since the disturbance d on y_r can be seen as a disturbance on r_r, thus exhibiting the same dynamics as the closed-loop system from r_r to y_r.

The second simulation focuses on testing the adaptivity of the control, *i.e.*, its robustness to process variations. The simulation is performed using the same input signal as the first simulation but without the ramp, and also increasing the gain of the plant $H_p^f(z)$ by 50 % at time 8, and subsequently decreasing the gain by 60 % at time 16. The result of the simulation is displayed in Figure 3.7. It is noted that the gain changes are only visible in the response of the relative position for one period of the square-wave. Further, since the gain of $H_p^f(z)$ increases, the system becomes faster and consequently less control signal is needed to achieve the desired response. This leads to less saturation and a higher value of α_k.

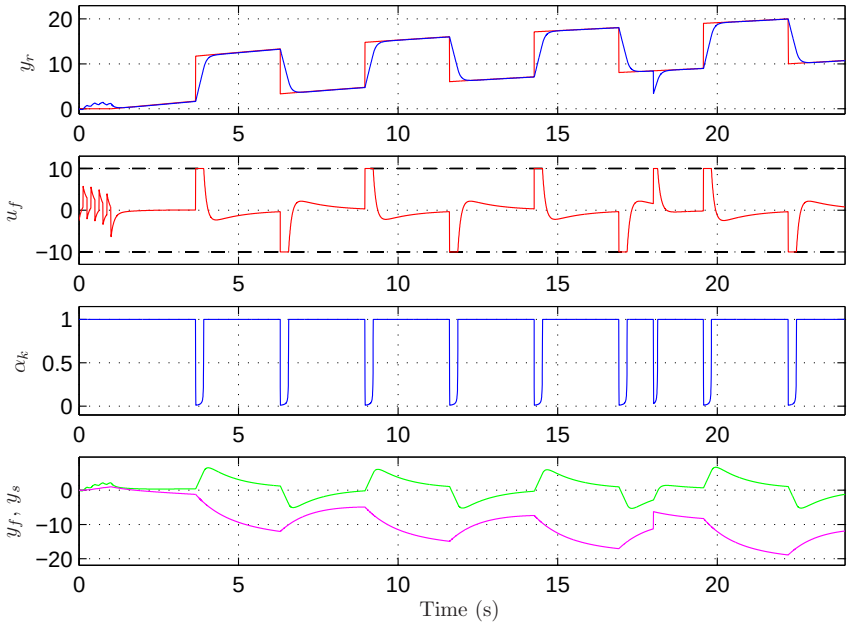

Figure 3.6 Simulation result of the AIMC controller subject to a ramped square-wave with a low-frequency sine wave superimposed as reference position (red curve in top plot). The relative position response is displayed in blue in the top panel, and the actuator positions in the bottom panel, where y_f is green and y_s is magenta. At time 18 s, the system is affected by a step position disturbance with amplitude 5.

The simulation results for the MVPC controllers compared to the proposed controller are presented together with the experimental results in Section 3.5, for cohesiveness.

3.4 Experimental Setup

The experimental setup used to evaluate the proposed control scheme is designed to be a small scale version, meant to emulate the macro/micro manipulator setup described Chapter 2. The setup consists of an ABB IRB2400 robot [ABB Robotics, 2013] with an S4CPlus controller, which acts as the macro manipulator system, and an ABB IRB120 robot [ABB Robotics, 2013] with an IRC5 controller, which is the micro manipulator system with high bandwidth. Naturally, both robots have saturation limits on velocity, but for proof of concept, the high bandwidth system is set to have an input saturation at ± 80 mm/s, and the macro manipulator system is assumed to be

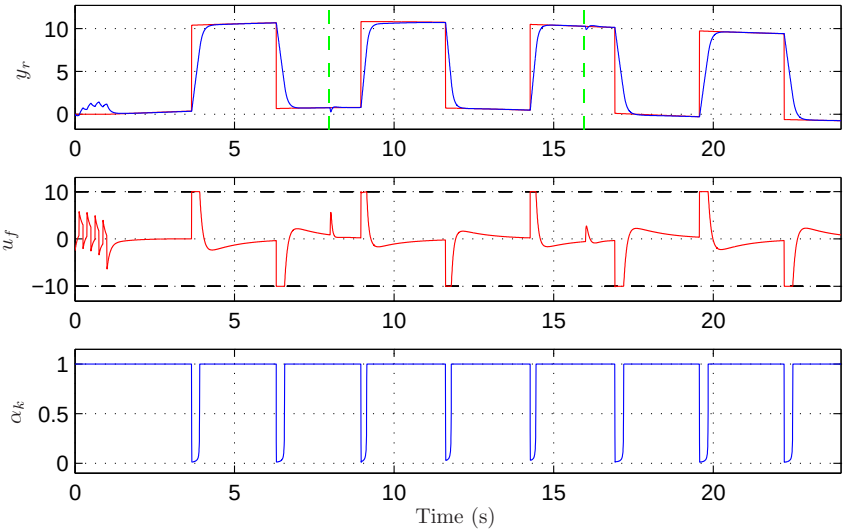

Figure 3.7 Simulation result of the AIMC controller subject to a square-wave with a sine wave superimposed as reference position (red curve in top plot). The relative position response is displayed in blue in the top panel. The dashed green lines indicate changes of process gain.

slow enough to not reach any saturation limits. In addition to the position measurements provided by the robot joint resolvers, the IRB120 robot is equipped with a Heidenhain linear encoder of model ST3078 [Heidenhain, 2013], which measures the relative distance between the two robot's end-effectors, with a measurement range of 26 mm at an accuracy of 2 µm. This measurement is essential in order to be able to compensate for arm-side position disturbances, that the motor-side robot joint resolvers are unable to measure. The IRB2400 robot is attached rigidly to the ground, while the IRB120 robot is attached to a base that can move in one direction, in order to introduce disturbances in the position, which frequently appear in the real milling setup.

The robots are interfaced using an open robot control extension of the conventional robot controller, called *ORCA* [Blomdell et al., 2010], running at 250 Hz. The MATLAB Simulink models were translated to *C*-code using *Real-Time Workshop* and compiled in order to run them on the robot system. A picture of the experimental setup is shown in Figure 3.8.

3.5 Experimental Results

Prior to performing experiments, dynamic models of the two robots, with Cartesian velocity reference as input and Cartesian position as output, were

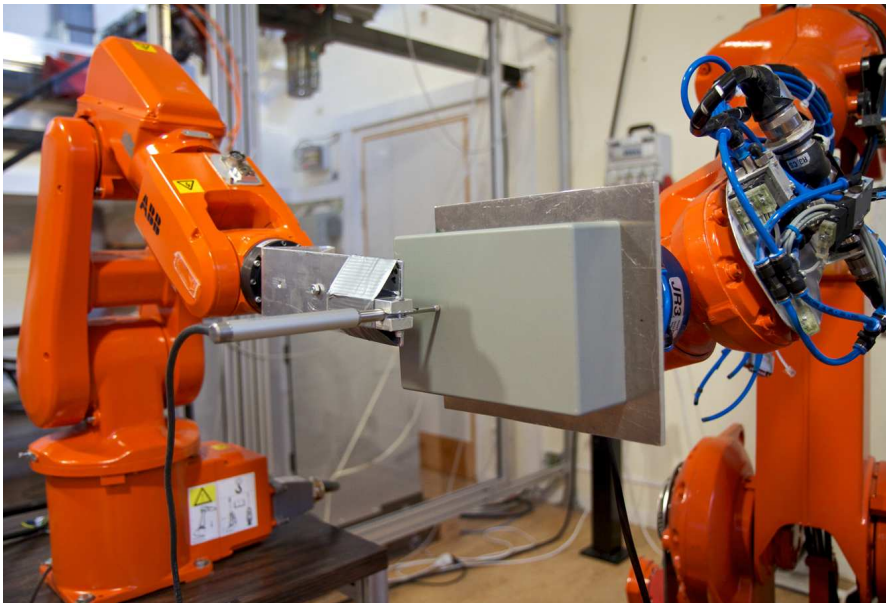

Figure 3.8 Experimental setup for performing mid-ranging control. The IRB120 robot (micro manipulator) holding the Heidenhain linear encoder is seen to the left, and the IRB2400 robot (macro manipulator) to the right.

identified in one axis using the Prediction Error Method [Johansson, 1993]. In order to provide excitation for the identification algorithm, a square-wave was used as reference, which is converted to joint motor angle velocity references, using the inverse Jacobian of the robot. The resulting measured Cartesian position of the robot was calculated using forward kinematics, and used as system output. Both robots exhibit similar dynamics, and the control loops that form H_{cl}^{f} and H_{cl}^{s}, were closed using proportional controllers such that the micro manipulator system had five times higher bandwidth than the macro manipulator system. New models of the closed-loop systems were calculated, resulting in third-order models, which were used as initial guesses in the RLS estimators. The online estimation of the models was evaluated before initiating the full AIMC control structure, by sending square-waves as position reference to the two robots. The results of the estimation procedure is displayed in Figure 3.9, where the bandwidth difference of the two systems is clearly illustrated. The desired complementary sensitivity functions T_f and T_s were chosen as first-order systems with bandwidth matching H_{cl}^{f} and H_{cl}^{s}, respectively.

The first experiment performed was designed to resemble the simulation in Figure 3.6, but since the linear encoder has limited measuring range, a

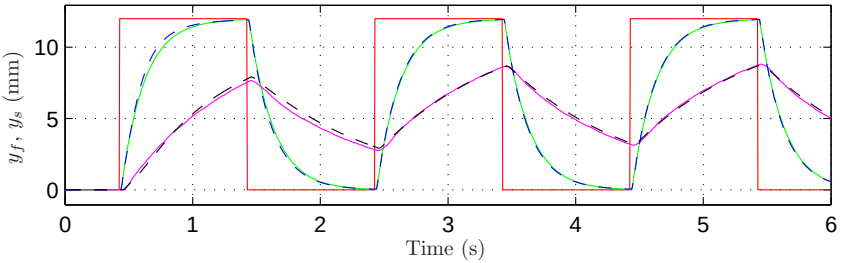

Figure 3.9 Estimation phase of the two systems, where y_f is green and y_s magenta. The estimates of these signals are denoted $\hat{y}_f$ and $\hat{y}_s$, and are shown in dashed blue and black, respectively.

ramp signal as input would leave that range rapidly. Thus, the relative position of the robots was instead calculated from the resolver measurements of the robots, so that a ramp signal could be used as input. The obtained result is displayed in Figure 3.10. It is evident from the figure that the desired mid-ranging effect is achieved, as well as that the control signal u_f is kept within its boundaries. A zoomed view of a step response from Figure 3.10 is displayed in Figure 3.11, where the desired response is also shown. It is noted that the response for the relative position y_r is close to the desired response. There is however an initial discrepancy, which appears because of the fact that the system has an input saturation. As displayed in the lower panel of Figure 3.11, the upper boundary on the control signal u_f has been reached, limiting the achievable bandwidth of the closed-loop system. It is to be noted that, given a perfect model of the system, the response of the system for any input signal would look the same, with and without the DRG. The control signal before the saturation, *i.e.*, u_f, would however, not be the same.

Additional experiments were performed in order to test how well the system handles position disturbances. For this purpose, the linear encoder was put into operation, replacing the resolver measurements for the relative position, so that disturbances in position can be measured and compensated for. The experiment was designed such that once the estimation phase finishes, the macro manipulator is controlled to move until the linear encoder is in the middle of its measurement range, which is set to be the zero position. The AIMC controller is then activated, with a square-wave as reference signal, while simultaneously moving the base with the micro manipulator, in order to introduce position disturbances. As mentioned earlier, the linear encoder only has a measurement range of 26 mm, and thus the amplitude of the relative position reference r_r was chosen to be 5 mm. Since a smaller amplitude of the reference results in less control signal, the desired bandwidth of T_f was increased by a factor of 5. The results of the experiment are shown in Figure 3.12. It is noted that under no disturbances, the system responds

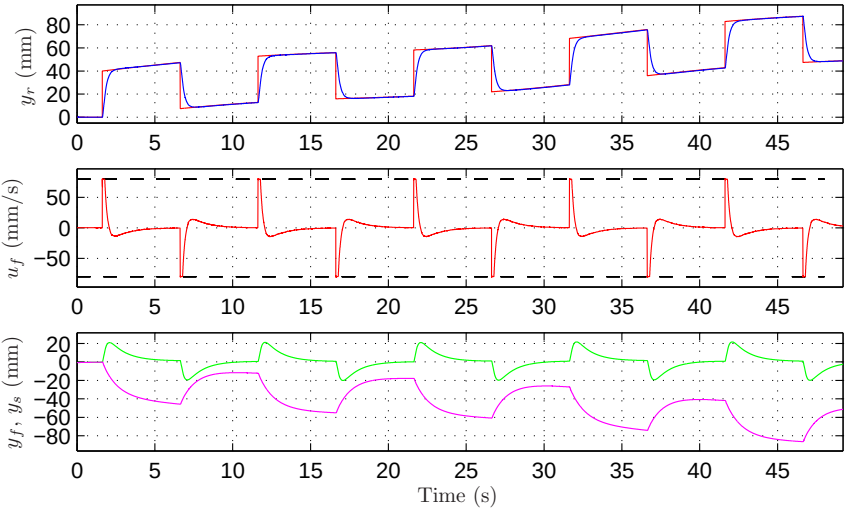

Figure 3.10 Experimental result of the AIMC controller subject to a ramped square-wave with a sine wave superimposed as reference position (red curve in top plot). The relative position y_r response is displayed in blue in the top panel, and the robot positions in the bottom panel, where y_f is green and y_s is magenta.

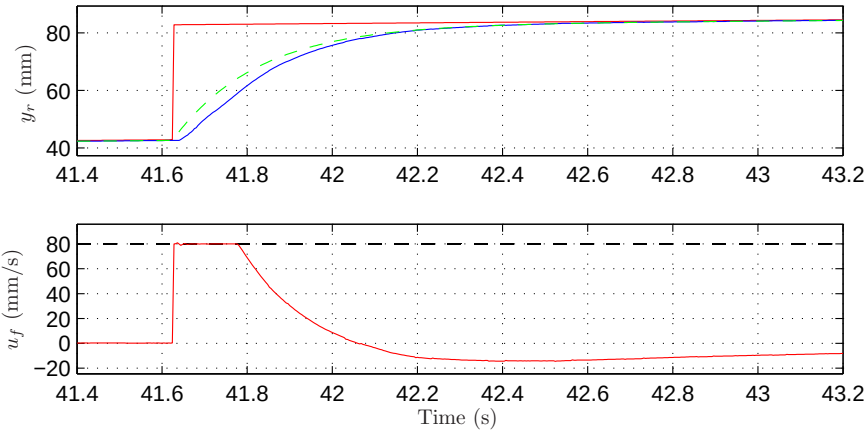

Figure 3.11 Zoomed view of the step after 40 s in Figure 3.10. The dashed green line shows the desired response of the system, *i.e.*, the response of $T_f(z)$.

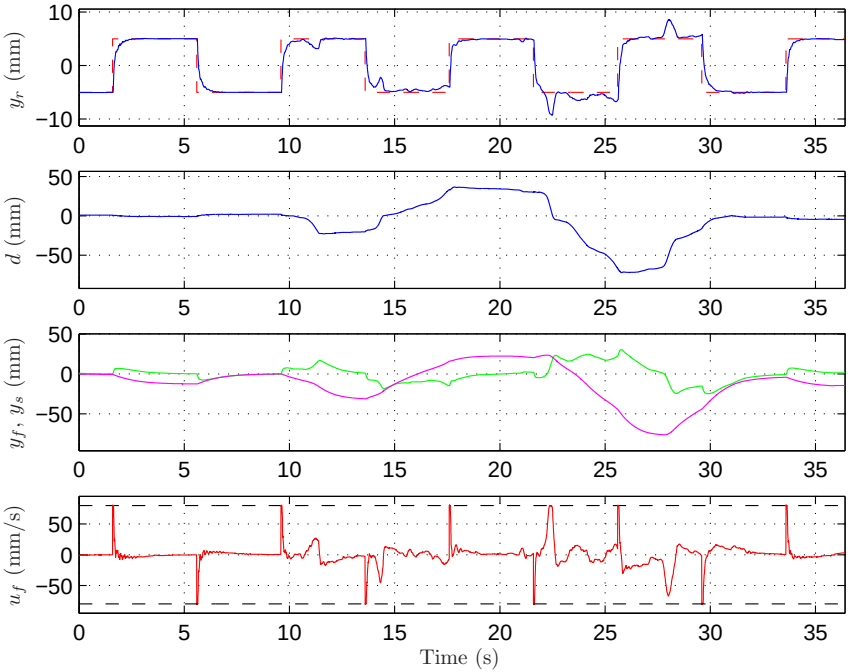

Figure 3.12 Experimental result of the AIMC controller with a square-wave as reference position (red curve in top plot), subject to position disturbances d as displayed in the second panel. The relative position y_r response is displayed in blue in the top panel, and the robot positions in the third panel, where y_f is green and y_s is magenta.

rapidly in a well-damped manner. When subject to continuous disturbances, the macro manipulator has to deviate further from its desired position, in order to cancel the disturbance. It does, however, eventually return to its midpoint.

In order to evaluate the performance of the proposed control scheme, the average Integrated Absolute Error (IAE) over several step responses was chosen to quantify the performance for the different controllers. The discrete-time approximation of the IAE is defined as

$$\text{IAE} = h \sum_{k=0}^{k_{\max}} |r_{r,k} - y_{r,k}|. \tag{3.19}$$

The MVPC controllers were tuned as described in Section 3.2. As the method suggests, model-order reduced versions of the previously identified models of H_{cl}^f and H_{cl}^s were used. The validity of the model-order reduced models

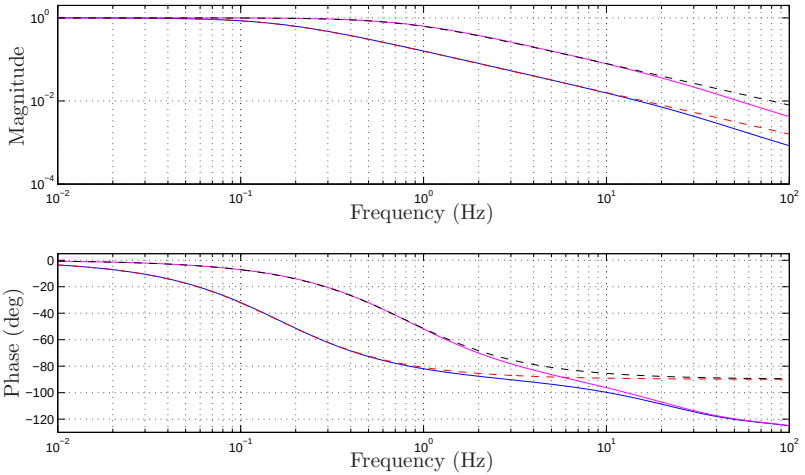

Figure 3.13 Bode diagram of the identified models H_{cl}^{f} (magenta) and H_{cl}^{s} (blue) and their model-order reduced counterparts, shown in dashed black and red, respectively.

Table 3.1 Normalized IAE value of step responses.

Setup	AIMC	MVPC+AW	MVPC
1. Sim, $r_r = 1.5$	1.000	1.525	1.525
2. Sim, $r_r = 5$	1.000	1.458	1.555
3. Sim, $r_r = 5$, noise	1.000	1.380	1.474
4. Exp, $r_r = 20$	1.000	1.344	1.353
5. Exp, $r_r = 30$	1.000	1.408	1.560

were investigated by looking at the Bode diagrams, as shown in Figure 3.13. The figure shows close correspondence for both models, in the frequency range of interest. The results of a series of simulations and experiments are presented in Table 3.1, where the IAE values have been normalized by the AIMC controller IAE value, in order to simplify comparison. The first setup was designed such that r_r is small enough to fulfill $|u_f| \leq u_{\text{sat}}$, whereas the following four setups were designed for the opposite. In the third setup, measurement noise was added in the simulation. It is to be noted that no process variation was present during the experiments presented in Table 3.1.

Experiments to test the robustness to process variations were performed by attaching a weight to the macro manipulator while running the controller.

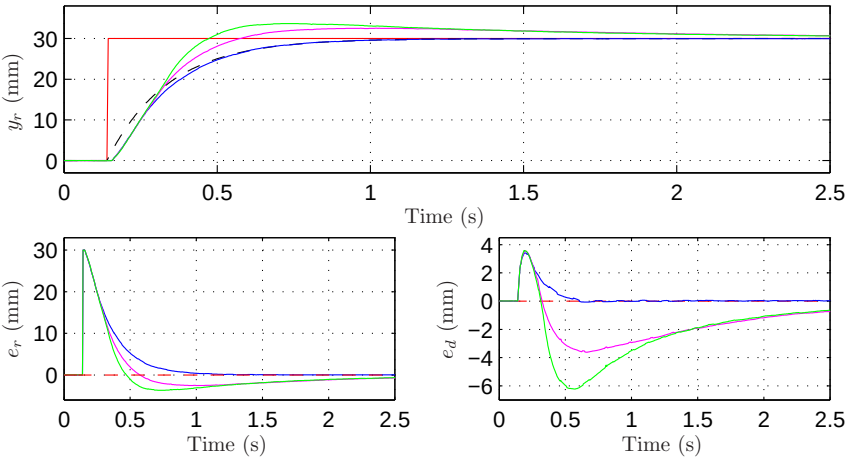

Figure 3.14 The top plot shows experimental step responses with $r_r = 30$, where the AIMC, MVPC+AW and MVPC controllers are shown in blue, magenta, and green, respectively. The desired step response is shown in dashed black. The bottom left plot shows the error between the reference and the responses, and the bottom right plot shows the error between the desired response and the responses.

However, even though the weight was close to as heavy as the maximum payload of the robot, no significant change in the process dynamics was observed. Instead, an artificial process variation was introduced by changing the gain of the input to H_{cl}^{f}. In a similar manner to the simulation studies, the gain was increased by 25 % and subsequently decreased by 30 %. The results of the experiment are shown in Figure 3.15. It is evident from the figure that the performance is deteriorated once the process changes, but in approximately three periods of the input signal, the system has adapted and the desired response is achieved. It is also noted that the DRG is efficient in keeping the constraints, even though considerable model errors occur during the adaptation to the process change.

3.6 Discussion and Conclusions

It was shown in simulations and verified through experiments that the proposed mid-ranging control structure for a macro and micro manipulator setup, performs satisfactory with a response close to the specification, while maintaining desired properties in the presence of internal saturations, process variations, and position disturbances. It is also noted that the obtained results from the simulations and experiments exhibit close correspondence.

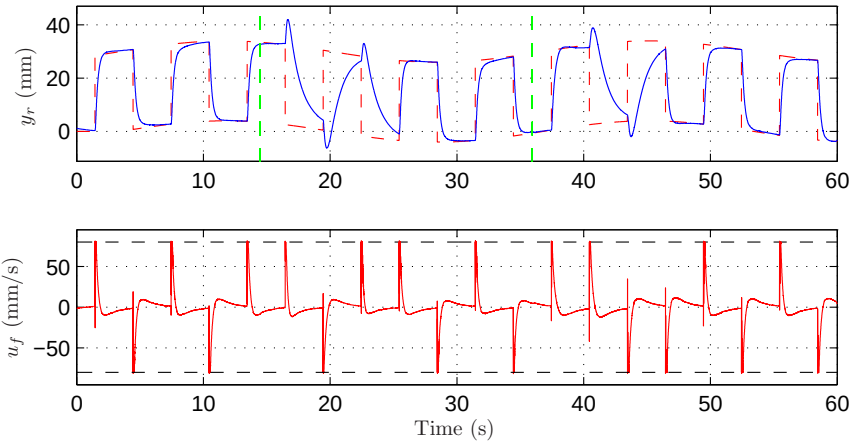

Figure 3.15 Experimental result of the AIMC controller subject to a ramped square-wave with a sine wave superimposed as reference position (red curve in top plot). The relative position y_r response is displayed in blue in the top panel. The dashed green lines indicate changes of process gain.

As shown in Table 3.1, the performance using the proposed controller compared to the MVPC controllers in the case of non time-varying processes, is increased by as much as 56 %. In the cases where process variations are present, the proposed controller will naturally perform significantly better than the MVPC controllers, due to its adaptive properties. Furthermore, looking at the error between the system response and the desired response, the achieved IAE was up to a factor 16 lower than that of the MVPC controller, as is clearly displayed in Figure 3.14. The performance of the MVPC controller is dependent on if it is possible to implement anti-windup schemes or not, but according to the original problem formulation in this chapter, it would not be possible. The MVPC controller without anti-windup will naturally perform worse for high-amplitude steps and high-frequency references, since the controller will be saturated more frequently. It could be possible to implement a DRG for the MVPC control scheme, similar to the proposed control scheme, in order to estimate the control signal for the anti-windup scheme. Since the purpose was to compare the proposed control to previously established methods, this is not considered. Further, it is noted that the performance of the proposed control scheme is deteriorated when subject to substantial measurement noise, since it corrupts the estimations of the models. This can be improved by increasing the forgetting factor to a value closer to 1, but will consequently result in slower adaptation to process variation. The proposed controller does, however, still perform 38 %–47 % better than the compared controllers.

When process variations were introduced, the system adapts quickly to

the new parameters, and the effects of the change can only be seen for a few periods of the input signal. It is, however, noted that the experimental results exhibit slightly slower adaptation with more pronounced transients than in simulation. This is caused by the fact that noise is present in the experiments, and as discussed earlier, the forgetting factor should be set to a higher value in order to reduce noise sensitivity. Additionally, the transients appear because of the increased complexity in estimating the parameters for a third-order model, as compared to the first-order models that are used in simulation. The adaptation of the system is dependent on the excitation of the input signal, with an input signal of high excitation, the system will adapt faster. Conversely, if the input signal is of low excitation, the system will adapt slowly and the transient performance will be poor.

The proposed adaptive DRG was proven to be effective, as seen in Figures 3.7, 3.11, and 3.15, the control signal is kept within the constraints, even under significant process variations. Even if no variations in the process dynamics are present, the adaptivity of the controller is still beneficial. This was demonstrated in Figure 3.9, where it is noted that the identified models are improved throughout the estimation procedure, thus increasing the performance of the closed-loop system.

The next step of this work will be to implement the proposed approach on the real milling experimental setup, and evaluate it in machining experiments. It is possible that the method needs modification in the case of low excitation in certain machining tasks. Further, it would be desirable to extend the method to account for the endpoints of the micro manipulator, such that they are never reached.

4

Deflection Compensation

4.1 Introduction

This chapter is based on the publication [Sörnmo et al., 2012b].

The problem of performing deflection compensation concerns machining operations where strong process forces are required. As discussed in previous chapters, serial industrial robots generally suffer from relatively low stiffness, which causes the robot to deviate from its desired path as a result of machining process forces. Since industrial robots can typically only measure position on the motor-side of the joint, as opposed to the arm-side, it is not possible to compensate for arm-side deflections that may occur. In order to compensate for these deflections, that lower the absolute accuracy, external sensors such as force/torque-sensors and tracking systems can be integrated in the robot system to be used in compensation schemes. In this chapter, deflection compensation to the purpose of increasing the absolute accuracy, using only the macro manipulator is considered.

Stiffness modeling and compensation is discussed in [Zhang et al., 2005], where a stiffness model of the robot in joint space is identified through load experiments. It was shown in a milling process that the accuracy of the surface was improved. Position compensation for the deflection of a compliant wrist, caused by external forces is considered in [Xu and Paul, 1988], where stability analysis and simulation results are presented. In [Roberts et al., 1985], it was shown that a mechanically compliant sensor can realize a more responsive force controlled system. Further, a compensation scheme for static position errors is developed.

In this chapter, two different methods for performing deflection compensation are evaluated; compensation based on a stiffness model of the robot and force feedback, and compensation using position feedback from an optical tracking system. The latter method is represented by the yellow jigsaw-piece in Figure 2.1; "Adaptive Tracking System".

4.2 Control Design

The aim of the deflection compensation is to continuously adjust the robot path, in order to suppress deviations in the actual traversed path, caused by machining process forces. The first approach to achieving this, utilizes a stiffness model of the robot to translate the measured process force to an estimated position deviation. A local Cartesian stiffness model is identified by applying a load on the robot, measuring the applied force and the deviation in robot position with an external measurement device, at several different points in the machining workspace. It is assumed that the Cartesian stiffness is linear in the region of expected milling process forces, and consequently, the stiffness in each point is determined by

$$f(t) = K_f x_p(t), \tag{4.1}$$

where $f(t)$ is the reaction force, K_f the stiffness and $x_p(t)$ the deflected distance. Values for intermediate points are determined by interpolation between measurements.

The compensation scheme uses the current position as measured by the robot, denoted z_m, to determine the current stiffness from the model. An estimated position error e_z, *i.e.*, the robot deflection, is calculated from the measured process force f_z, in the same direction as the force. Since a positive force will result in a deflection in the same direction, the compensation should be actuated in the opposite direction of the force. The deflection is used as input to a velocity controller $C(s)$, that is designed as a low-pass filtered proportional controller. The cut-off frequency of the low-pass filter is set to a magnitude lower than the bandwidth of the robot, in order not to act on high-frequency errors that the robot is unable to compensate for, because of its limited structural bandwidth compared to its controlled bandwidth. For the same reason, the gain of the controller is set to a low value in order not to amplify noise. The controller calculates a velocity reference v_r, which is converted to joint space using the inverse Jacobian of the robot, and integrated to a modified position reference. Both velocity and position references are continuously sent to the internal robot joint controllers. A block diagram for the force feedback deflection compensation is displayed in Figure 4.1.

The second approach to compensating for robot position deflections, relies on measurements from an optical tracking system that measures the Cartesian arm-side position of the robot. By subtracting the arm-side Cartesian position of the robot z_a, from the desired Cartesian position of the robot z_d, as obtained through forward kinematics using the current position reference to the joints, a position error is formed. This error is used as input to a velocity controller, identical to the controller described for the force feedback method. A block diagram for the position feedback deflection compensation is displayed in Figure 4.2.

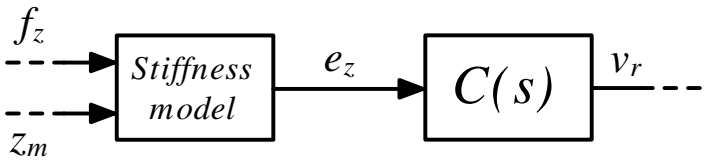

Figure 4.1 Block diagram for the closed-loop system with force feedback deflection compensation.

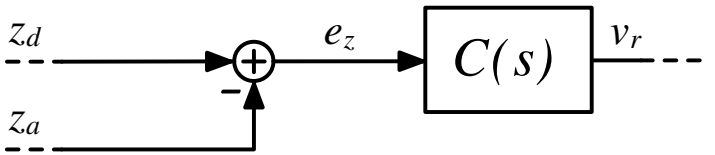

Figure 4.2 Block diagram for the closed-loop system with arm-side position feedback deflection compensation.

4.3 Experimental Setup

Experiments were performed using an ABB IRB2400-robot [ABB Robotics, 2013] with an S4CPlus controller, using an open robot control extension called *ORCA* [Blomdell et al., 2010], running at 250 Hz. The MATLAB Simulink models were translated to *C*-code using *Real-Time Workshop* and compiled in order to run them on the robot system. The robot was equipped with a flange-mounted JR3 force/torque sensor of model 100m40AI63 [JR3, 2013], measuring forces and torques in the Cartesian directions at a sampling rate of 8 kHz.

Face milling experiments were performed with the workpiece attached to the robot end-effector. A Teknomotor spindle was rigidly attached to a base, with a 6 mm milling tool running at 24 000 rpm. Since the robot position is normally calculated from the joint angles on the motor side of the gear-box, it is not possible to measure deviations on the arm side. A Nikon K600 optical tracking system [Nikon Metrology, 2010] was used, by attaching infrared LED markers on the robot, so that the actual position of the end-effector could be measured. The tracking system has an approximate accuracy of ± 40 µm, and was calibrated to collect measurements in the same frame as the robot. The experimental setup for milling is displayed in Figure 4.3, and the tracking system can be seen in Figure 4.4.

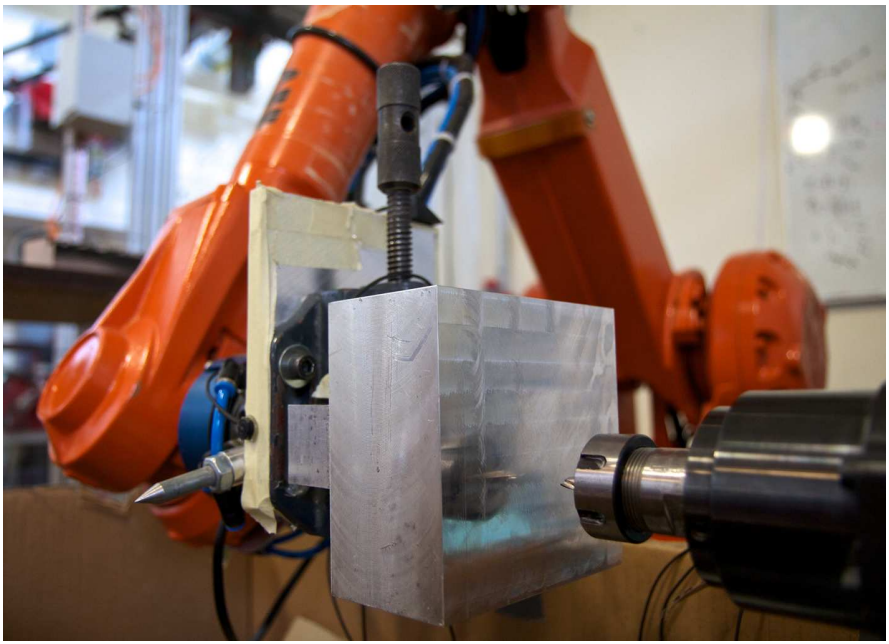

Figure 4.3 The experimental setup for performing deflection compensated milling with an ABB IRB2400 robot.

Figure 4.4 The Nikon K600 optical tracking system.

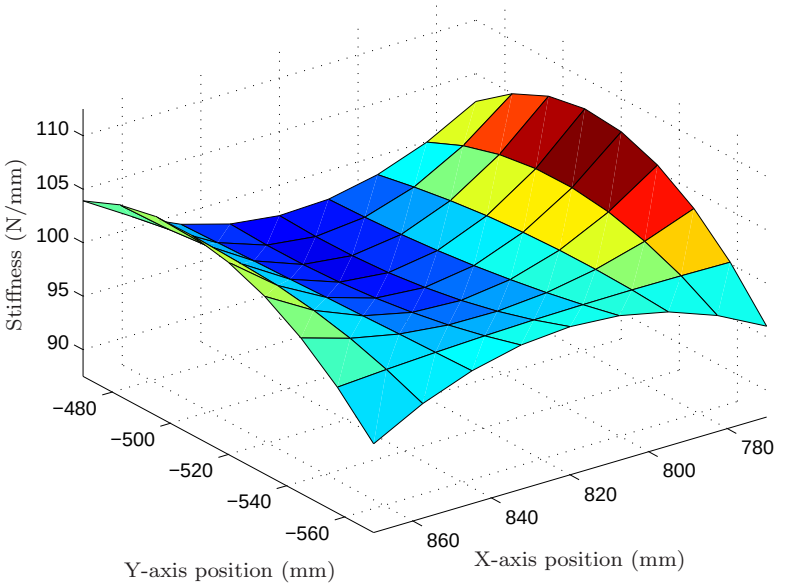

Figure 4.5 A subset of the robot stiffness measurements along the Z-axis.

4.4 Experimental Results

Prior to performing milling experiments, the Cartesian stiffness model of the robot was experimentally identified, following the method described in Section 4.2. A subset of the stiffness measurements is shown in Figure 4.5, where it can be seen that the robot stiffness only varies approximately within the range ±5 N/mm in the milling workspace.

Using the identified stiffness model the control scheme for deflection compensation was implemented, and both compensated and uncompensated face milling experiments were performed in a block of Aluminium (Al 7075) with a depth-of-cut of 3 mm and feed rate of 10 mm/s. In these experiments, the optical tracking system was only used to measure the actual robot position, in order to validate the method. The results of the uncompensated and compensated milling experiments are shown in blue and red, respectively, in Figure 4.6. It is evident from the figure that the resulting process force of the milling gives a significant position deviation. Further, it can be seen that the deflection compensation is successful in suppressing the process force induced position deviation. It is, however, not possible to compensate for other position errors with this method. This is possible to see in Figure 4.6, as both position error curves exhibit similar profiles, although centered around different levels.

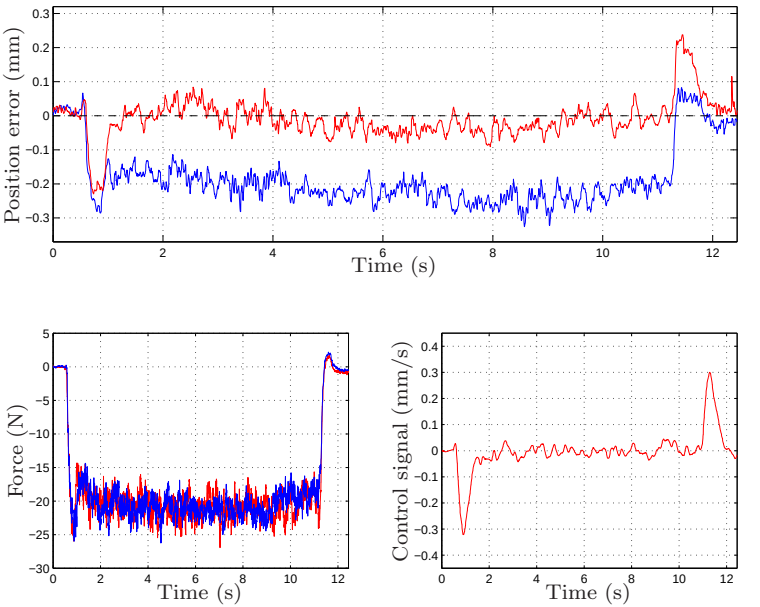

Figure 4.6 Face milling in aluminium, with force feedback deflection compensation. The upper panel displays position error in the direction perpendicular to the feed rate, where blue is the uncompensated case and red is the compensated. The lower left plot shows the process force, and the lower right plot shows the deflection compensation control signal.

Similar experiments as described above were performed using the position feedback-based controller, where measurements from the optical tracking system were used as feedback. The results of the uncompensated and compensated case are shown in Figure 4.7. It is noted that the position error for the compensated case is centered around zero, and that all errors in position, not only process force induced deviations, are compensated. This is further tested in a milling scenario where the calibration between the tracking system and the robot frame is not accurate. This results in a linear drift in the measured position as compared to the desired position. The compensated and uncompensated case are shown in Figure 4.8, where it is clearly illustrated that the drift is compensated by the position feedback.

Since the aim of the proposed methods is to increase the absolute accuracy of the milling task, the normalized IAE is an appropriate measure to quantify this. The normalized discrete-time IAE is here defined as

$$\text{IAE} = \frac{1}{n}\sum_{k=1}^{n} |z_d - z_a|. \tag{4.2}$$

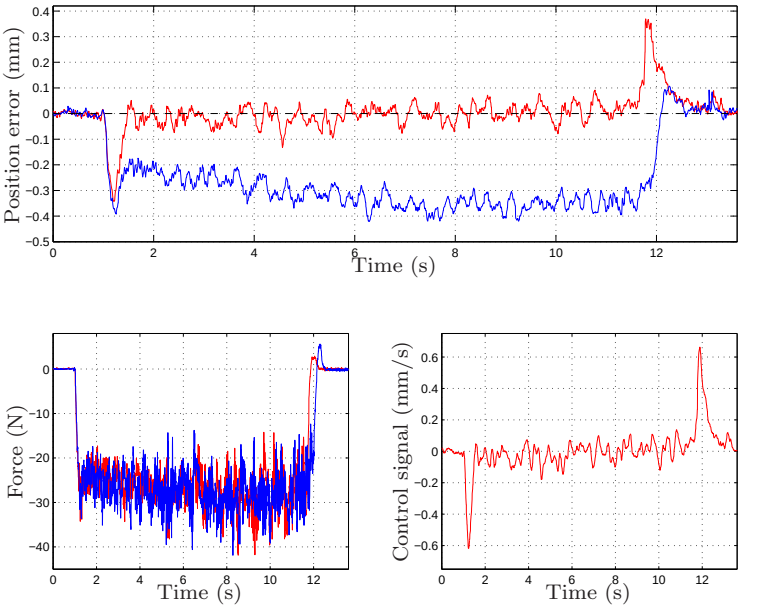

Figure 4.7 Face milling in aluminium, with arm-side position feedback. The upper panel displays position error in the direction perpendicular to the feed rate, where blue is the uncompensated case and red is the compensated. The lower left plot shows the process force, and the lower right plot shows the deflection compensation control signal.

Table 4.1 Normalized IAE of milling results using force feedback (FF) and position feedback (PF).

	Uncompensated	**Compensated**	**Ratio**
FF IAE (μm)	218.7	36.3	6.0
PF IAE (μm)	246.5	27.2	9.1

Table 4.1 shows the IAE values for the uncompensated and compensated cases for both proposed deflection compensation schemes.

4.5 Discussion

It was shown in face milling experiments that both proposed deflection compensation schemes effectively increased the absolute accuracy, by real-time

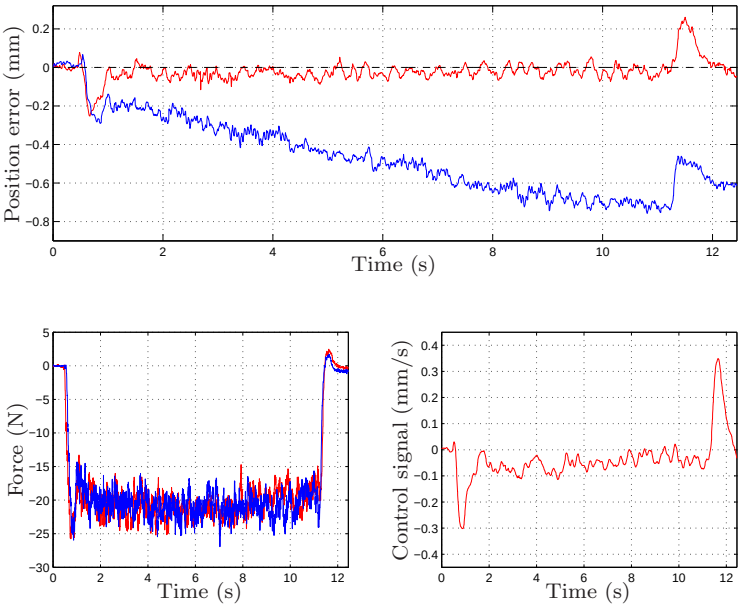

Figure 4.8 Face milling in aluminium, with arm-side position feedback and inaccurate calibration. The upper panel displays position error in the direction perpendicular to the feed rate, where blue is the uncompensated case and red is the compensated. The lower left plot shows the process force, and the lower right plot shows the deflection compensation control signal.

modification of the robot path. The IAE for the force feedback deflection compensation was reduced by a factor of approximately 6, compared to the uncompensated case. This indicates that the identified stiffness model is accurate throughout the milling workspace. The IAE of the position feedback compensation was reduced by a factor of approximately 9. The additional increase in accuracy, compared to the force feedback method, is most likely due to the fact that the arm-side position feedback method also can compensate for position deviations not induced by process forces, such as calibration errors. Furthermore, the position feedback does not rely on a stiffness model, which is advantageous should the stiffness vary. However, the use of an optical tracking system for milling is not always advantageous, since chips that are emitted continuously from the milling process might obscure the camera. In the scenario considered in this chapter, this was not a problem and caused at most an occasional outlier in the measurements. In more violent milling processes, however, this can pose a serious problem. Also, in advanced milling tasks, the robot configuration may be such that the LED-markers are

obscured from view. In these cases, the force feedback method would be advantageous to use since it is not affected by this.

It was noted in the experiments that a faster feed rate, resulted in a larger perpendicular process force, and thus, a larger deviation of the robot position. Consequently, the benefit of utilizing deflection compensation will be even greater for high-speed machining processes. In the case of using force feedback compensation, this will lead to increased requirements on the accuracy of the stiffness model, since model errors will be magnified with strong process forces.

5

Force Controlled Feed Rate Adaptation

5.1 Introduction

This chapter is based on the publication [Sörnmo et al., 2012b].

In machining processes, the robot is required to come into physical contact with the work object. If the contact force is too strong, the task will not be executed properly. Conversely, if the force is too weak, the task will not be performed time-efficiently. Traditionally, robotic machining tasks have been performed using position feedback with a conservative feed rate so as not to exceed the maximum allowed force, *e.g.*, defined by the tool breaking or scorching the material. By controlling the applied force, realized by adjusting the feed rate of the workpiece, precise control over the material removal can be exercised. If the maximum allowed force is used as reference, this will in turn lead to maximization of the time-efficiency of the machining task, since the maximum amount of material can be removed per time unit.

Here, the control problem of machining a workpiece with unknown surface, while striving to maintain the desired force reference, is considered. The problem can be reformulated as adjusting the feed rate of the workpiece in order to achieve the desired force. The machining process forces are a nonlinear function of several parameters, such as spindle speed, machining tool, depth-of-cut, and material stiffness. Since some of these parameters are likely to change during the machining process, it is desirable to continuously adapt the force controller. The use of a fixed controller may result in poor performance and stability problems.

Force control for industrial manipulators performing contact-tasks is discussed in [Hogan and Buerger, 2005]. It was shown that the environment, *i.e.*, the work object, can be modeled as an admittance, whereby it follows that the robot should act as an impedance in the closed kinematic chain.

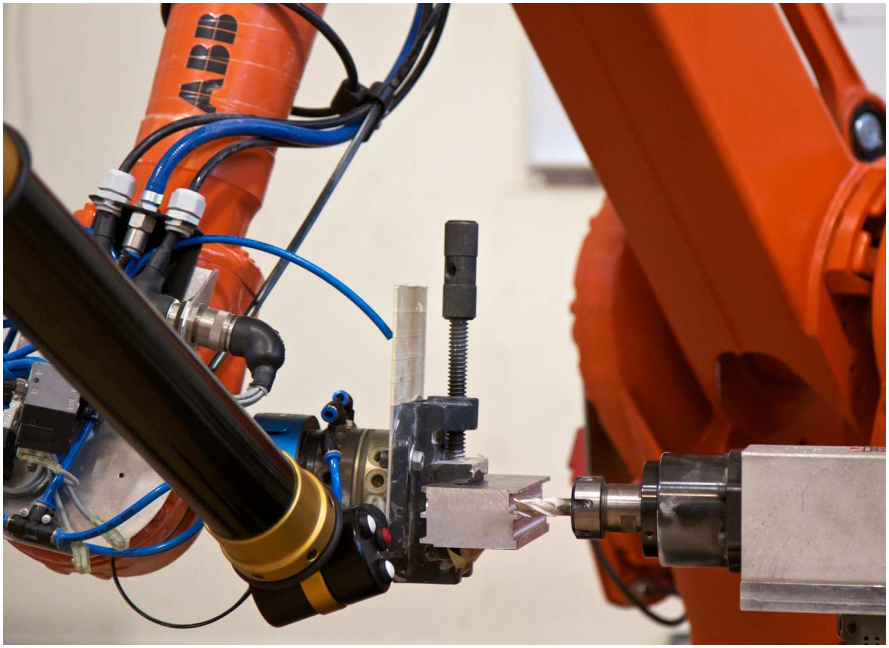

Figure 5.1 The experimental setup for performing force controlled milling with an ABB IRB2400 robot.

Hence, the aim of impedance control for robots is to control the dynamic relation between the force and the position.

A self-tuning PI controller for controlling machining forces was presented in [He et al., 2007], where the machining force is modeled as a static nonlinear relation between the feed rate and the depth-of-cut. In [Liu et al., 2001], an adaptive control constraint is considered, based on several control structures such as PID control, neural network control, and fuzzy control. An overview of force control technologies in machining is provided in [Wang et al., 2008]. One established method is the maximum material removal controller, which switches between discrete feed rate levels in order to maintain an approximate force reference. In contrast, it should be noted that the controller presented in this chapter continuously adapts the feed rate in order to achieve the desired force reference value.

In this chapter, a model-based adaptive force controller for machining processes is presented. The machining force dynamics is modeled as a linear system with a time-varying parameter, estimated such that the proposed controller is adapted to different machining conditions.

5.2 Modeling and Control Design

Along the feed direction of the machining, the aim is to control the milling force by adjusting the feed rate, which in robotic machining corresponds to the velocity of the robot end-effector. A model with velocity reference v_r as input, and actual velocity v in the Cartesian space as output, was identified from experimental data from the robot, using subspace-based system identification methods [Overschee and De Moor, 1994]. The corresponding continuous-time transfer function is given by

$$G_v(s) = \frac{b_2 s^2 + b_1 s + b_0}{s^3 + a_2 s^2 + a_1 s + a_0}. \tag{5.1}$$

The milling process forces depend on several parameters, as mentioned earlier. These parameters exhibit a nonlinear relationship with the process force and may change over time, thus making the process difficult to model. Here, a first-order model is derived, with a time-varying parameter to the purpose of capturing the nonlinear properties and changes in the process parameters. By assuming that the machined material is linear-elastic and isotropic, the model is derived using Hooke's law

$$f(t) = K_f x_p(t), \tag{5.2}$$

where $f(t)$ is the force, K_f the material stiffness, and $x_p(t)$ the depth of the deformation into the material. Since the material is assumed to be isotropic, the material stiffness K_f is constant throughout the workpiece. By assuming that material is removed at a rate proportional to the integral of the applied force, the following relation holds

$$f(t) = K_f \left(x_p(t) - \int_0^t D_f^{-1} f(\tau)\, \mathrm{d}\tau \right), \tag{5.3}$$

where D_f denotes the *material removal parameter*. It is obvious from (5.3), that a large value of D_f will result in a slow material removal rate and thus a large machining force.

Transforming (5.3) to the frequency-domain and substituting position for velocity gives

$$F(s) = \frac{K_f D_f s}{s D_f + K_f} X_p(s) = \underbrace{\frac{K_f D_f}{s D_f + K_f}}_{G_f(s)} V(s), \tag{5.4}$$

where the transfer function from v to f is denoted $G_f(s)$. The complete transfer function $G_f(s)G_v(s)$, from velocity reference to force is now given by a fourth-order system. A linear-quadratic (LQ) optimal control scheme

[Zhou and Doyle, 1998] is proposed, which is superior to a standard PID controller in its ability to increase the bandwidth of the closed-loop system. In addition, the LQ control scheme can effectively attenuate resonances which are likely to be present in the robot dynamics. The robot dynamics $G_v(s)$ can be expressed as a state-space model of the innovations form

$$\dot{x}(t) = Ax(t) + Bv_r(t) + Ke(t) \tag{5.5}$$
$$v(t) = Cx(t) + e(t), \tag{5.6}$$

where K is the Kalman gain which is provided by the system identification algorithm and $e(t)$ is white noise. Since the states of the robot dynamics are not measurable, a Kalman filter (KF) [Kalman, 1960] is introduced in order to estimate the states, based on the measured velocity and the identified model. The Kalman filter equations are given by

$$\dot{\hat{x}}(t) = A\hat{x}(t) + Bv_r(t) + K(v(t) - C\hat{x}(t)) \tag{5.7}$$
$$\hat{v}(t) = C\hat{x}(t) \tag{5.8}$$

where $\hat{x}$ is the estimated state vector. Since the model is identified with experimental data with subtracted mean, the filter is extended with a constant *disturbance state* [Åström and Wittenmark, 1997] in order to achieve the correct static gain.

The complete model for the system is obtained by augmenting the state-space model in (5.5)–(5.6) with the force dynamics given in (5.4). Since the force can be measured, it is favorably chosen as a state. By introducing $x_f(t) = f(t)$ and differentiating (5.3), the following relation is obtained

$$\dot{x}_f(t) = -K_f {D_f}^{-1} x_f(t) + K_f v(t). \tag{5.9}$$

Further, the input $v(t)$ is given by the output from the robot dynamics in (5.6), which inserted into (5.9) gives

$$\dot{x}_f(t) = -K_f {D_f}^{-1} x_f(t) + K_f C x(t) + K_f e(t). \tag{5.10}$$

By defining the new output as the force and the extended state vector as $x_e(t)$, the augmented state-space model can be written as

$$\dot{x}_e(t) = \begin{bmatrix} \dot{x}(t) \\ \dot{x}_f(t) \end{bmatrix} = \begin{bmatrix} A & 0 \\ K_f C & -K_f {D_f}^{-1} \end{bmatrix} \begin{bmatrix} x(t) \\ x_f(t) \end{bmatrix} + \begin{bmatrix} B \\ 0 \end{bmatrix} v_r(t) + \begin{bmatrix} K \\ K_f \end{bmatrix} e(t) \tag{5.11}$$

$$f(t) = \begin{bmatrix} 0 & 0 & 0 & 1 \end{bmatrix} \begin{bmatrix} x(t) \\ x_f(t) \end{bmatrix} + w(t), \tag{5.12}$$

where $w(t)$ is white noise.

The state feedback control law is given by

$$v_r(t) = -L \begin{bmatrix} \hat{x}(t) \\ x_f(t) \end{bmatrix} + l_r f_r(t), \tag{5.13}$$

where $f_r(t)$ is introduced as the desired force and l_r is the feedforward gain. The gain vector L is determined by LQ optimal control, *i.e.*, by minimizing the cost function

$$J(x_e, v_r) = \int_0^\infty x_e(t)^T Q x_e(t) + v_r(t)^T R v_r(t) \, \mathrm{d}t, \tag{5.14}$$

where Q and R are user-defined weights. The optimal value of L is calculated by solving the *algebraic Riccati equation* [Zhou and Doyle, 1998].

In order to eliminate possible stationary errors, integral action is introduced by extending the state vector with the integral state

$$x_i(t) = \int_0^t (f_r(\tau) - f(\tau)) \, \mathrm{d}\tau. \tag{5.15}$$

With this extra state, the gain vector L has to be extended as well. Hence, $L_e = \begin{bmatrix} L & l_i \end{bmatrix}$, where l_i is the integral state gain, is defined.

The controller has so far been derived assuming a constant D_f. As discussed earlier, the material removal parameter D_f is likely to be time-varying and should thus be estimated continuously. This is accomplished by utilizing recursive estimation methods, such as the recursive least-squares (RLS) algorithm or a Kalman filter [Johansson, 1993]. In this study, the RLS algorithm, as given in (3.5)–(3.7), has been utilized.

When the covariance of the estimate passes below a desired threshold, the controller is activated and the estimate of D_f can be used to continuously adapt the controller. This is done by updating the model in (5.11) using the current estimate of D_f, and subsequently calculating the gain vector of the LQ controller by minimizing (5.14) for the new system. A block diagram for the complete closed-loop system is displayed in Figure 5.2.

5.3 Simulation Results

Simulations were performed using MATLAB Simulink, by discretizing and implementing the models and control scheme described in the previous section. The feed rate controller is tuned by adjusting the weights Q and R in (5.14), so that the cost will be high if the machining force deviates from the desired value, resulting in a fast force response. For the simulations, a material stiffness K_f of 50 N/mm was assumed, and the initial value for the material

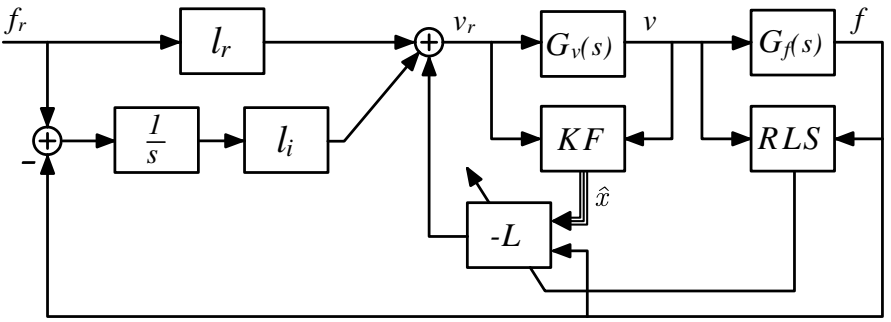

Figure 5.2 Block diagram for the closed-loop system using the feed rate controller.

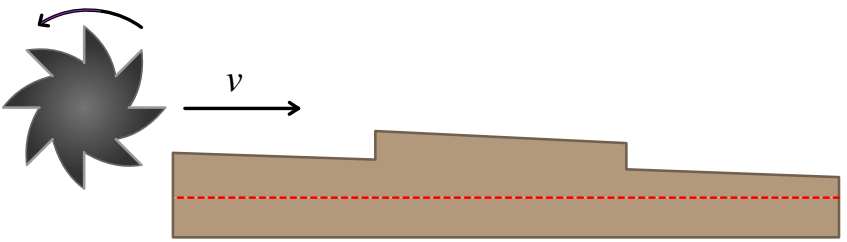

Figure 5.3 The peripheral milling scenario with a varying depth-of-cut.

removal parameter D_f was set to 1. In order to obtain a feasible estimate of D_f before the adaptive LQ controller is activated, the velocity reference is initially set to a conservative constant velocity so as to provide excitation for the estimation algorithm. Once the estimation covariance passes below a threshold, the velocity reference is switched to the now activated adaptive controller.

The material removal is set to be time-varying, both with step changes in D_f and continuously decreasing D_f. The scenario can be considered to resemble a milling experiment with a varying depth-of-cut, which is illustrated in Figure 5.3.

This scenario is considered in a milling simulation with the force control loop active, using an initial speed of 6 mm/s and a desired force of 20 N. The result of the simulation is displayed in Figure 5.4. The activation of the controller is indicated by the force reference (dashed blue line) being set to the given value. It is evident from Figure 5.4 that the adaptive controller can compensate for step changes in D_f, as well as a continuously decreasing D_f, in a fast, well-damped manner.

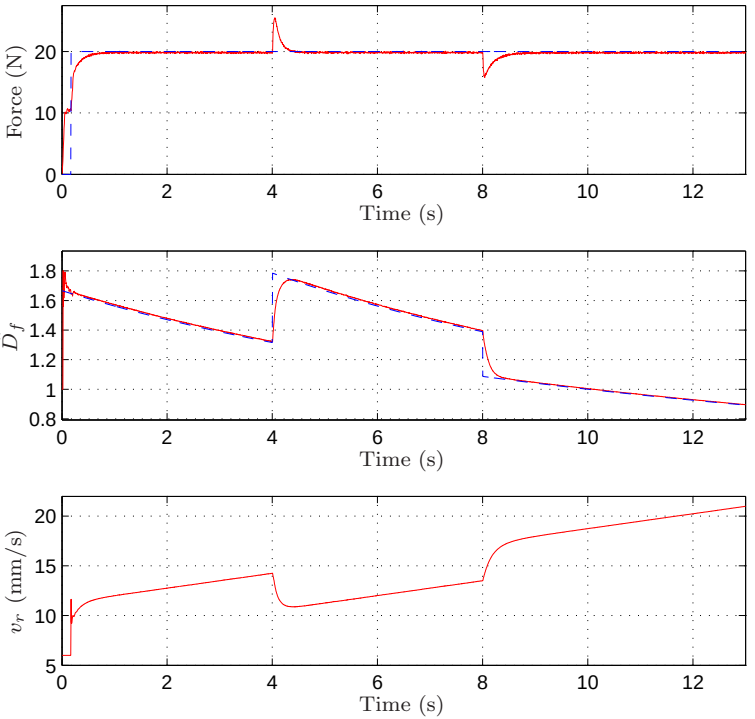

Figure 5.4 Milling simulation using adaptive force control, with a time-varying D_f.

5.4 Experimental Setup

Experiments were performed using an ABB IRB2400 robot [ABB Robotics, 2013] with an S4CPlus controller, using an open robot control extension called *ORCA* [Blomdell et al., 2010], running at 250 Hz. The MATLAB Simulink models were translated to *C*-code using *Real-Time Workshop* and compiled in order to run them on the robot system. The robot was equipped with a flange-mounted JR3 force/torque sensor of model 100m40AI63 [JR3, 2013], measuring forces and torques in the Cartesian directions at a sampling rate of 8 kHz. A CimCore measurement arm of model Stinger II, as seen in Figure 5.1, was used to obtain position measurements with an accuracy of approximately 50 µm.

Peripheral milling experiments were performed using a workpiece of Cibatool material, attached to the robot end-effector. A Teknomotor spindle was rigidly attached to the base, with a 14 mm milling tool running at 24 000 rpm. The experimental setup is displayed in Figure 5.1.

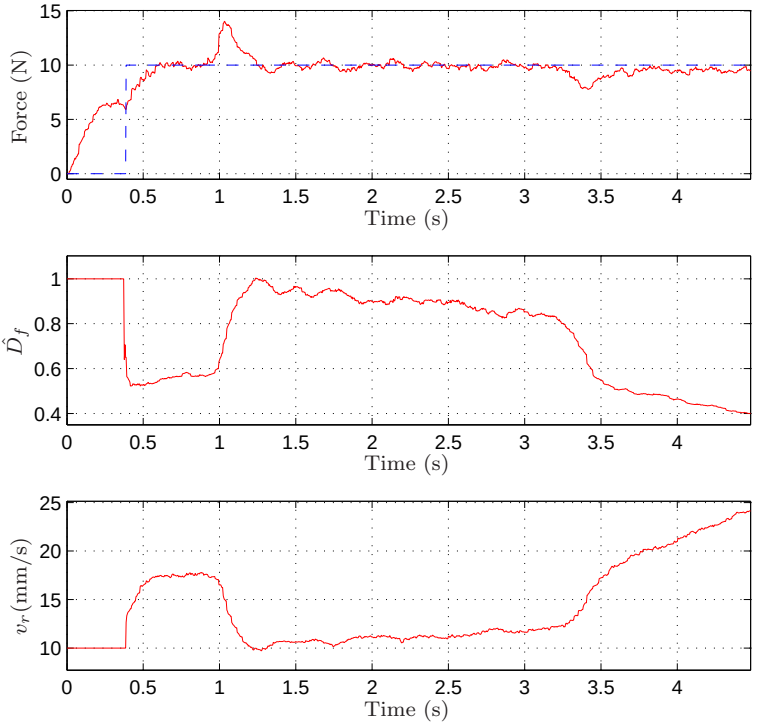

Figure 5.5 Experimental peripheral milling using adaptive force control, with a time-varying depth-of-cut.

5.5 Experimental Results

In the experiments, the material stiffness K_f was interpreted as the *interaction stiffness*, due to the fact that the machining force not just depends on the material properties, but on the combined stiffness of the workpiece, the tool, and the robot. It is to be noted that the stiffness of the robot in this context refers to the perceived robot stiffness, as determined from the robot position measurements. It is further assumed that the interaction stiffness is constant within the limited workspace of the milling process. By measuring force and position of the robot during a simple contact experiment, the interaction stiffness was estimated to 85 N/mm.

In order to emulate the milling scenario described in Section 5.3, the workpiece was manually prepared so as to resemble the profile illustrated in Figure 5.3. The milling was performed with an initial v_r of 10 mm/s, a force reference of 10 N and an initial value of D_f set to 1. The result is displayed in Figure 5.5. As in the simulation, the experimental force response is fast and

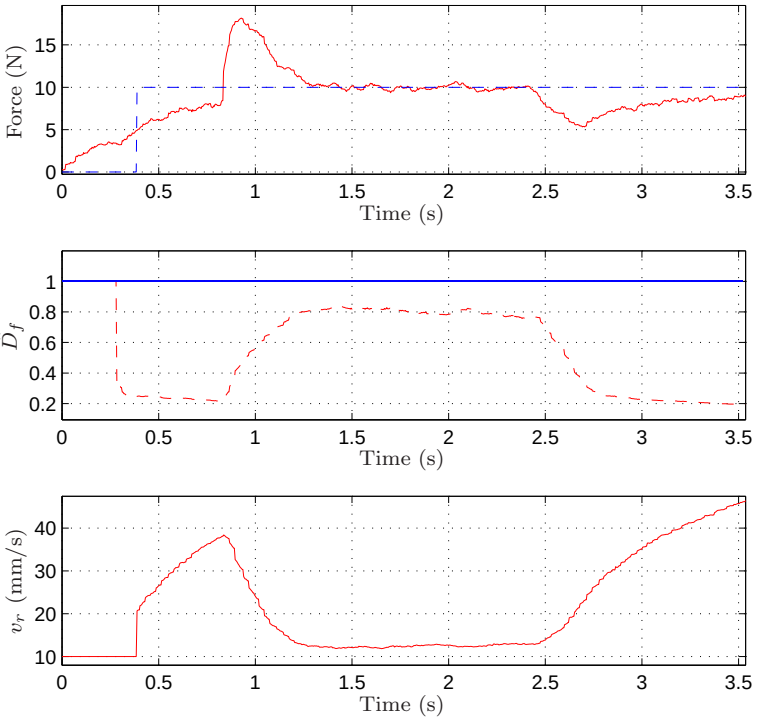

Figure 5.6 Force controlled peripheral milling without adaptation for material removal, with a time-varying depth-of-cut. The middle panel shows the nominal D_f (blue) vs. the estimated D_f (red).

robust to both step changes in D_f as well as to a continuously decreasing D_f.

To demonstrate the benefit and necessity of adapting the force controller, the milling experiment described above was repeated with a force controller with fixed parameters, disabling the estimation of D_f and assuming it to be constant with a value of 1. The results in Figure 5.6 clearly show that the system becomes slow for a D_f not close to the assumed value, and does not handle step changes in D_f satisfactorily.

In order to further test the flexibility of the controller, face milling experiments were performed in aluminium (Al 7075), where the interaction stiffness K_f was significantly higher than in Cibatool, with a value of 143 N/mm. The result of a face milling with a depth-of-cut of 1 mm and a force reference of 50 N is displayed in Figure 5.7. It is noted that the estimation of D_f requires slightly more time to pass the estimation variance threshold. Furthermore, the steady-state value of D_f is much higher and the force response is faster

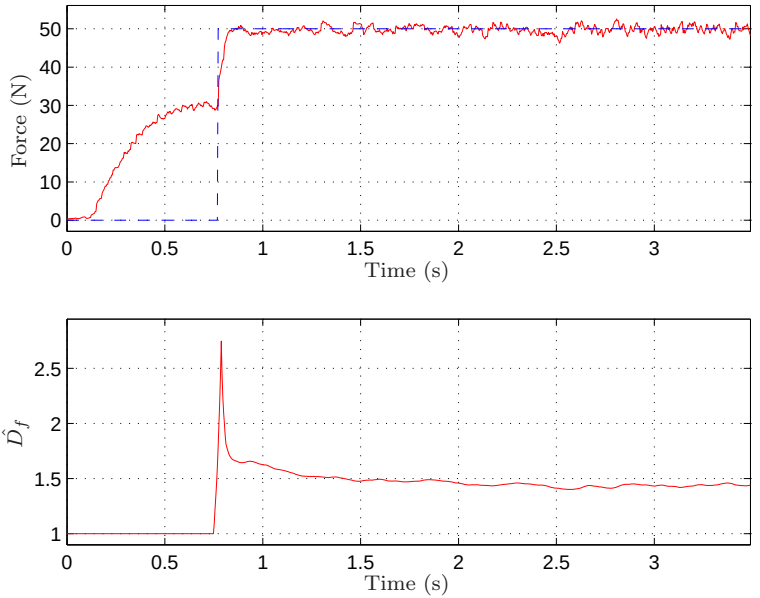

Figure 5.7 Force controlled face milling in aluminium, with a constant depth-of-cut.

than in the Cibatool material, which is to be expected since aluminium is significantly stiffer.

5.6 Discussion

This chapter has described a method for force feedback-based feed rate control in robotic machining processes, removing the maximum amount of material per time unit by adaptively controlling the applied force. It was shown in two different milling processes and materials, that the proposed controller is effective in maintaining the desired force reference under varying cutting conditions. Further, it was shown that the adaptation of the controller is essential for good performance with time-varying machining parameters. With a non-adaptive force controller, a conservative force reference would have to be used in order not to exceed the maximum allowed force, because of the large overshoots that occur at abrupt depth-of-cut changes. This will in turn result in a slower feed rate, and thus, longer execution times to perform the task.

6

Conclusions

This thesis has presented control methods for improving machining processes performed using industrial robots. To the purpose of increasing the accuracy of machining tasks, a macro/micro manipulator setup was considered, where modeling and control of the micro manipulator was presented. Position control and milling experiments were performed to verify the effectiveness of the proposed control structure. Control errors as well as workpiece surface accuracies within the desired accuracy of ± 50 μm were achieved. The compensated milling experiments reached up to three times higher surface accuracy than the uncompensated case, looking at both maximum error and standard deviation.

A mid-ranging control structure was proposed for the macro/micro manipulator setup, where the manipulators were closed-loop controlled, containing internal velocity saturations. An adaptive solution was presented, where simulation and experimental results using a smaller scale setup, exhibit close correspondence. It was shown that the proposed control structure performs well in the presence of process variations, internal saturations and position disturbances, with a performance increase of up to 56 % to that of the compared previously established methods.

Two different deflection compensation schemes were introduced, based on force and arm-side position feedback, respectively. Both methods were shown to effectively increase the absolute accuracy of milling experiments. The IAE values from the desired profiles were decreased by factors 6 and 9, for the force and position feedback methods, respectively.

An adaptive, model-based force control architecture for feed rate control in robotic machining processes was presented. Both simulations and milling experiments were performed using the proposed controller, and it was shown to be effective in maintaining the desired force reference under varying cutting conditions. Further, a comparison between the controller with and without parameter adaptation was performed, and it was concluded that adaptation is essential for good performance in milling processes with varying parameters, such as depth-of-cut.

Bibliography

ABB Robotics (2013). *ABB IRB120 Industrial Robot Data sheet*. Data sheet nr. ROB0149EN_D.

ABB Robotics (2013). *ABB IRB2400 Industrial Robot Data sheet*. Data sheet nr. PR10034 EN_R7.

Abele, E., J. Bauer, T. Hemker, R. Laurischkat, H. Meier, S. Reese, and O. von Stryk (2011). "Comparison and validation of implementations of a flexible joint multibody dynamics system model for an industrial robot". *CIRP J. Manufacturing Science and Technology* **4**:1, pp. 38–43.

Al Janaideh, M, Y. Feng, S. Rakheja, C.-Y. Su, and C. Alain Rabbath (2009). "Hysteresis compensation for smart actuators using inverse generalized Prandtl-Ishlinskii model". In: *Proc. Am. Control Conf.* St. Louis, MO, pp. 307–312.

Allison, B. and A. Isaksson (1998). "Design and performance of mid-ranging controllers". *J. Process Control* **8**:5, pp. 469–474.

Allison, B. and S. Ogawa (2003). "Design and tuning of valve position controllers with industrial applications". *Trans. of the Institute of Measurement and Control* **25**:1, pp. 3–16.

Åström, K. J. and B. Wittenmark (1997). *Computer-Controlled Systems*. Prentice Hall, Englewood Cliffs, NJ.

Bemporad, A. (1998). "Reference governor for constrained nonlinear systems". *IEEE Trans. on Automatic Control* **43**:3, pp. 415–419.

Blomdell, A., I. Dressler, K. Nilsson, and A. Robertsson (2010). "Flexible application development and high-performance motion control based on external sensing and reconfiguration of ABB industrial robot controllers". In: *Proc. Workshop of "Innovative Robot Control Architectures for Demanding (Research) Applications—How to Modify and Enhance Commercial Controllers", IEEE Int. Conf. Robotics and Automation*. Anchorage, Alaska, USA, pp. 62–66.

COMET (2013). EU/FP7-project: *Plug-and-produce COmponents and METhods for adaptive control of industrial robots enabling cost effective, high precision manufacturing in factories of the future*, URL: http://www.cometproject.eu.

Datta, A. and J. Ochoa (1996). "Adaptive internal model control: design and stability analysis". *Automatica* **32**:2, pp. 261–266.

dSPACE GmbH (2007). *DS1103 PPC Controller Board—Hardware Installation and Configuration*. dSPACE GmbH, Paderborn, Germany.

Economou, C., M. Morari, and B. Palsson (1986). "Internal model control: extension to nonlinear system". *Industrial & Engineering Chemistry Process Design and Development* **25**:2, pp. 403–411.

Fasse, E and N Hogan (1995). "Control of physical contact and dynamic interaction". In: *Proc. 7th Int. Symp. Robotics Research*. Munich, Germany, pp. 28–38.

Garcia, C. and M. Morari (1982). "Internal model control. a unifying review and some new results". *Industrial & Engineering Chemistry Process Design and Development* **21**:2, pp. 308–323.

Gayadeen, S. and W. Heath (2009). "An internal model control approach to mid-ranging control". *IFAC Advanced Control of Chemical Processes* **7**:part 1.

Ge, P. and M. Jouaneh (1996). "Tracking control of a piezoceramic actuator". *IEEE Trans. Control Syst. Technol.* **4**:3, pp. 209–216.

Gilbert, E., I. Kolmanovsky, and K. Tan (1995). "Discrete-time reference governors and the nonlinear control of systems with state and control constraints". *Int. J. of Robust and Nonlinear Control* **5**:5, pp. 487–504.

Haugwitz, S., M. Karlsson, S. Velut, and P. Hagander (2005). "Anti-windup in mid-ranging control". In: *Proc. 44th IEEE Conf. on Decision and Control and European Control Conf.* Seville, Spain.

Haverkamp, B and M Verhaegen (1997). *SMI Toolbox: State Space Model Identification Software for Multivariable Dynamical Systems*. Delft University of Technology, Delft, The Netherlands.

He, J., Z. Pan, and H Zhang (2007). "Adaptive force control for robotic machining process". In: *Proc. Am. Control Conf.* New York City, NY, pp. 1–6.

Heidenhain (2013). URL: http://www.heidenhain.com.

Hogan, N. and S. P. Buerger (2005). *Impedance and Interaction Control, Robotics and Automation Handbook*. CRC Press, Boca Raton, FL, pp. 19–1–19–24.

Hu, Q. and G. Rangaiah (1999). "Adaptive internal model control of nonlinear processes". *Chemical Engineering Science* **54**:9, pp. 1205–1220.

Hunt, K. and D. Sbarbaro (1991). "Neural networks for nonlinear internal model control". In: *Control Theory and Applications, IEE Proc. D.* Vol. 138. 5. IET, pp. 431–438.

Johansson, R. (1993). *System Modeling and Identification*. Prentice Hall, Englewood Cliffs, NJ.

JR3 (2013). URL: http://www.jr3.com.

Kalman, R. E. (1960). "A new approach to linear filtering and prediction problems". *Trans. of the ASME—J. of Basic Engineering* **82**:D, pp. 35–45.

Keyence Corp. (2006). *LK-G Series User Manual*. Keyence Corp., Osaka, Japan.

Krejci, P. and K. Kuhnen (2001). "Inverse control of systems with hysteresis and creep". In: *IEE Proc. Control Theory and Applications*. Vol. 148. 3, pp. 185–192.

Li, Y. and Q. Xu (2011). "A totally decoupled piezo-driven XYZ flexure parallel micropositioning stage for micro/nanomanipulation". *IEEE Trans. Automation Science and Eng.* **8**:20, pp. 265–279.

Liaw, H. C. and B. Shirinzadeh (2010). "Constrained motion tracking control of piezo-actuated flexure-based four-bar mechanisms for micro/nano manipulation". *IEEE Trans. Automation Science and Eng.* **7**:3, pp. 699–705.

Liu, Y., T. Cheng, and L. Zuo (2001). "Adaptive control constraint of machining process". *Int. J. Adv. Manufacturing Tech.* **17**, pp. 720–726.

Ljung, L. (2010). *System Identification Toolbox 7: Users's Guide*. The MathWorks, Inc., Natick, Massachusetts.

Mahr GmbH (2011). *MarSurf M 400 Flyer*. Mahr GmbH, Göttingen, Germany.

MathWorks Inc. (2010). *Real-Time Workshop 7: Users's Guide*. The MathWorks, Inc., Natick, Massachusetts.

Menold, P. H., R. K. Pearson, and F Allgöwer (1999). "Online outlier detection and removal". In: *Proc. of the 7th Mediterranean Conf. on Control and Automation*, pp. 1110–1133.

Nikon Metrology (2010). *K-series optical CMM solutions*. Data sheet Optical_CMM_EN_0311.

Olofsson, B. (2013). *Topics in Machining with Industrial Robots and Optimal Control of Vehicles*. Licentiate Thesis ISRN LUTFD2/TFRT--3259--SE. Department of Automatic Control, Lund University, Sweden.

Olofsson, B., O. Sörnmo, U. Schneider, A. Robertsson, A. Puzik, and R. Johansson (2011). "Modeling and control of a piezo-actuated high-dynamic compensation mechanism for industrial robots". In: *IEEE/RSJ Int. Conf. on Intelligent Robots and Systems*. San Francisco, CA, pp. 4704–4709.

Overschee, P van and B De Moor (1994). "N4SID: subspace algorithms for the identification of combined deterministic-stochastic systems". *Automatica* **30**:1, pp. 75–93.

Puzik, A, A Pott, C. Meyer, and A Verl (2009). "Industrial robots for machining processes in combination with an additional actuation mechanism for error compensation". In: *7th Int. Conf. on Manufacturing Research*. University of Warwick, United Kingdom.

Puzik, A, C. Meyer, and A Verl (2010). "Results of robot machining with additional 3D-piezo-actuation-mechanism for error compensation". In: *7th CIRP Int. Conf., Intelligent Computation in Manufacturing Eng.: Innovative and Cognitive Production Technology and Systems*. Capri, Italy.

Puzik, A. (2011). *Genauigkeitssteigerung bei der spanenden Bearbeitung mit Industrierobotern durch Fehlerkompensation mit 3D Ausgleichsaktorik*. PhD dissertation. University of Stuttgart, Stuttgart, Germany.

Reis GmbH (2011). *Reis RV40 Fact Sheet*. Reis GmbH, Obernburg, Germany.

Roberts, R., R. Paul, and B. Hillberry (1985). "The effect of wrist force sensor stiffness on the control of robot manipulators". In: *Proc. 1985 IEEE Int. Conf. on Robotics and Automation*. Vol. 2, pp. 269–274.

Schneider, U. (2010). *Regelung einer 3D-Ausgleichsaktorik für Fräsanwendungen mit Industrierobotern*. Diploma Thesis. Fraunhofer Institute for Manufacturing and Engineering, Stuttgart, Germany.

Sharon, A. and D. Hardt (1984). "Enhancement of robot accuracy using endpoint feedback and a macro-micro manipulator system". In: *Am. Control Conf., 1984*. IEEE, pp. 1836–1845.

Sharon, A., N. Hogan, and D. E. Hardt (1993). "The macro/micro manipulator: an improved architecture for robot control". *Robotics & Computer-Integrated Manufacturing* **10**:3, pp. 209–222.

Silva, G. and A. Datta. "Adaptive internal model control: the discrete-time case". In: *Proc. of the 1999 Am. Control Conf.* Vol. 1. IEEE. San Diego, CA, pp. 547–555.

Sörnmo, O., B. Olofsson, U. Schneider, A. Robertsson, and R. Johansson (2012a). "Increasing the milling accuracy for industrial robots using a piezo-actuated high-dynamic micro manipulator". In: *2012 IEEE/ASME Int. Conf. on Advanced Intelligent Mechatronics*. Kaohsiung, Taiwan, pp. 104–110.

Sörnmo, O., B. Olofsson, A. Robertsson, and R. Johansson (2012b). "Increasing time-efficiency and accuracy of robotic machining processes using model-based adaptive force control". In: *10th Int. IFAC Symposium on Robot Control*. Dubrovnik, Croatia, pp. 543–548.

Sörnmo, O., B. Olofsson, A. Robertsson, and R. Johansson (2013). "Adaptive internal model control for mid-ranging of closed-loop systems with internal saturation". In: *IEEE/RSJ Int. Conf. on Intelligent Robots and Systems*. Tokyo, Japan. Submitted.

Verhaegen, M and P Dewilde (1992). "Subspace model identification—The output-error state-space model identification class of algorithms". *Int. J. Control* **56**, pp. 1187–1210.

Vuong, N. D., M. H. Ang Jr., T. M. Lim, and S. Y. Lim (2009). "Multi-rate operational space control of compliant motion in robotic manipulators". In: *Proc. of 2009 IEEE Int. Conf. on Systems, Man and Cybernetics*, pp. 3175–3180.

Wang, J., G. Zhang, H. Zhang, and T. Fuhlbrigge (2008). "Force control technologies for new robotic applications". In: *IEEE Int. Conf. Tech. for Practical Robot Applications*. Woburn, MA, pp. 143–149.

Wiener, N. (1949). *The Extrapolation, Interpolation, and Smoothing of Stationary Time Series with Engineering Applications*. Originally issued as a classified MIT Rad. Lab. Report in February, 1942. Wiley, New York.

Xu, Y. and R. Paul (1988). "On position compensation and force control stability of a robot with a compliant wrist". In: *Proc. of the 1988 IEEE Int. Conf. on Robotics and Automation,* vol. 2. Philadelphia, PA, pp. 1173–1178.

Zhang, H., J. Wang, G. Zhang, Z. Gan, Z. Pan, H. Cui, and Z. Zhu (2005). "Machining with flexible manipulator: toward improving robotic machining performance". In: *Proc. IEEE/ASME Int. Conf. Adv. Intelligent Mechatronics*. Monterey, California, USA, pp. 1127–1132.

Zheng, A., V. Mayuresh, and M. Morari (1994). "Anti-windup design for internal model control". *Int. J of Control* **60**:5, pp. 1015–1024.

Zhou, K. and J. Doyle (1998). *Essentials of robust control*. Prentice Hall, Upper Saddle River, NJ.